UNIVERSITY OF LJUBLJANA
FKKT
Faculty of Chemistry and Chemical Technology

Carbon Materials for Energy Storage and Conversion

Synthesis and Characterization of Graphene-Based Derivatives

LAB COURSE – Instructions

Miha NOSAN, Maris Minna MATHEW, Boštjan GENORIO

Ljubljana, 2024

Synthesis and Characterization of Graphene-Based Derivatives — LAB COURSE - instructions

Avtorji: Miha Nosan, Maris Minna Mathew, Bostjan Genorio

Study materials for the programme - Carbon Materials for Energy Storage and Conversion

Strokovni pregled: prof. dr. Miran Gaberšček, izr. prof. dr. Nejc Hodnik

Oblikovanje in prelom: Dušan Komel

Slike in risbe: Miha Nosan, Maris Minna Mathew, Ivo Bardarov, Desislava Apostolova

Jezikovni pregled: Terry Troy Jackson

Urednica založbe: izr. prof. dr. Barbara Modec

Založila: Univerza v Ljubljani, Fakulteta za kemijo in kemijsko tehnologijo

Za založbo: prof. dr. Andreja Žgajnar Gotvajn

1. spletna izdaja

Ljubljana, 2024

Kataložni zapis o publikaciji (CIP) pripravili v Narodni in univerzitetni knjižnici v Ljubljani

COBISS.SI-ID 192814595

ISBN 978-961-7078-43-5 (PDF)

url: https://fkkt.uni-lj.si/fileadmin/user_upload/o_fakulteti/e_gradiva/Synthesis_and_Characterization_of_Graphene-Based_Derivatives-2024-Nosan-Mathew-Genorio.pdf

Table of Contents

Introduction

Throughout the history of planet Earth, it has undergone countless changes, some gradual, others cataclysmic. In recent decades, however, a self-inflicted crisis has taken shape that threatens to irreversibly alter the balance of our biosphere. This threat is none other than global warming. As the concentration of greenhouse gases in our atmosphere has increased, primarily due to the burning of fossil fuels (industry, energy production, industrial processes, etc.), deforestation, agricultural practices, and waste management, the average temperature of the Earth has increased.[1,2,3]

The consequences of this rising temperature are more frequent and severe heat waves, higher sea levels, melting glaciers, the disruption of ecosystems and biodiversity, and the increased release of greenhouse gases captured by the sea. Faced with these challenges, humanity is in an urgent race against time to find sustainable solutions that can help mitigate the effects of global warming and restore ecological balance. One promising solution lies in the field of alternative energy sources.[2]

Alternative energies have emerged as important solutions to counteract the environmental impact of traditional fossil fuels. Solar and wind energy are renewable and clean energy sources, but they depend on weather conditions and daytime, making them unpredictable. Among others, geothermal, tidal, and hydroelectric energy, while effective, are site-specific and usually tend to disrupt local ecosystems.[4,5,6]

Finally, the intricate web of energy systems, electrochemical energy, has emerged as the central thread that connects the principles of chemistry, physics, and engineering. At its core, electrochemical energy refers to the processes by which chemical energy is converted to electrical energy or stored, primarily through redox reactions (batteries, fuel cells) and capacitance or pseudo-capacitance (supercapacitors). This energy storage or conversion, which is fundamental to devices such as batteries, fuel cells, and supercapacitors, plays a leading role in numerous applications, from powering our smartphones to storing energy for entire power grids. The appeal of electrochemical energy lies in the direct conversion between chemical and electrical forms, often with high efficiency and the ability to store or provide energy on demand. As the world grapples with the challenges of climate change and the need for sustainable energy solutions, the role of electrochemical systems has never been clearer. Their potential to interconnect with renewable energy sources and provide clean energy storage and delivery mechanisms makes electrochemical energy at the forefront of green energy sources.[6]

In energy storage systems (ESS), the diffusion of ions is pivotal for energy storage and conversion, as evidenced by various ESS device types. Batteries, for example, exhibit relatively slow ion diffusion, resulting in lower power density compared to capacitors, which allow fast ion movement. With their rapid energy release, capacitors can support fuel cells and batteries during high energy demand, potentially extending the life of ESSs. Ideally, ESSs should achieve both high energy and power density, underscoring their importance.[4]

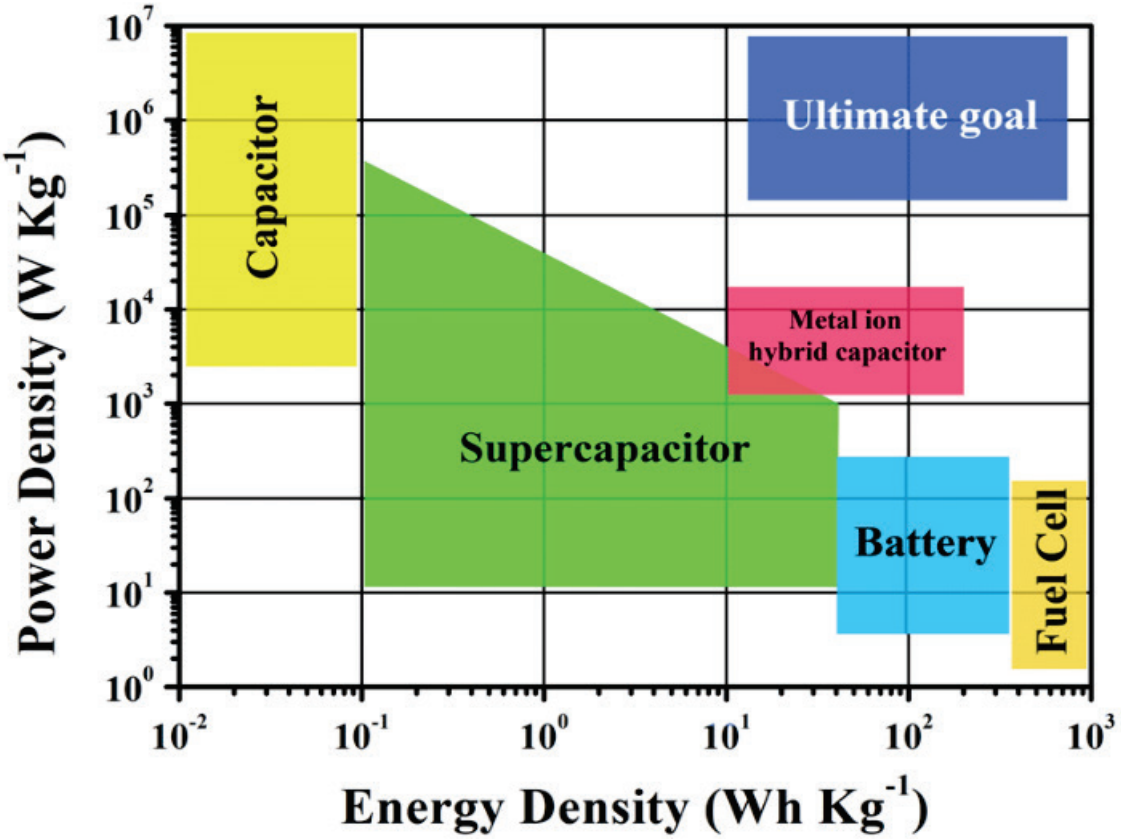

Figure 1: Ragone plot of energy storage and conversion devices.[7]

Figure 1 shows that capacitors have high power density but are limited in energy density. In contrast, fuel cells and batteries are known for their high energy density. Supercapacitors, interestingly, close the gap between batteries and conventional capacitors on the Ragone diagram. While ESS offers many advantages, their performance is inevitably limited by the properties of their active materials which should be low-cost and durable.

Among the ESS, the fuel cell functions as an energy converter that continuously converts the chemical energy of a fuel into electricity. These devices offer superior characteristics compared to conventional combustion-based systems currently used in several major sectors, including electronics, households, power generation plants, transportation, and the military. They outperform internal combustion engines in terms of efficiency, with energy conversion rates of over 60% and minimal emissions. Most importantly, hydrogen fuel cells produce only water as a byproduct, avoiding the release of carbon dioxide and other pollutants that contribute to smog and health problems. Fuel cells can operate continuously as long as a constant supply of fuel is available. They are also quieter when operating since they are built from stationery units, unlike combustion engines.[6]

Although there are different types of fuel cells, they all basically work in a similar way as the proton-exchange membrane fuel cell shown in **Figure 2**. They usually consist of three main components: the anode, the electrolyte, and the cathode. At the anode, fuel undergoes an

oxidation reaction that produces cations, which move across the electrolyte to the cathode while simultaneously releasing free electrons. These electrons flow outward and combine with oxygen at the cathode. The energy liberated during the electrochemical reaction of fuel and oxidant is converted to electrical energy.[4,5]

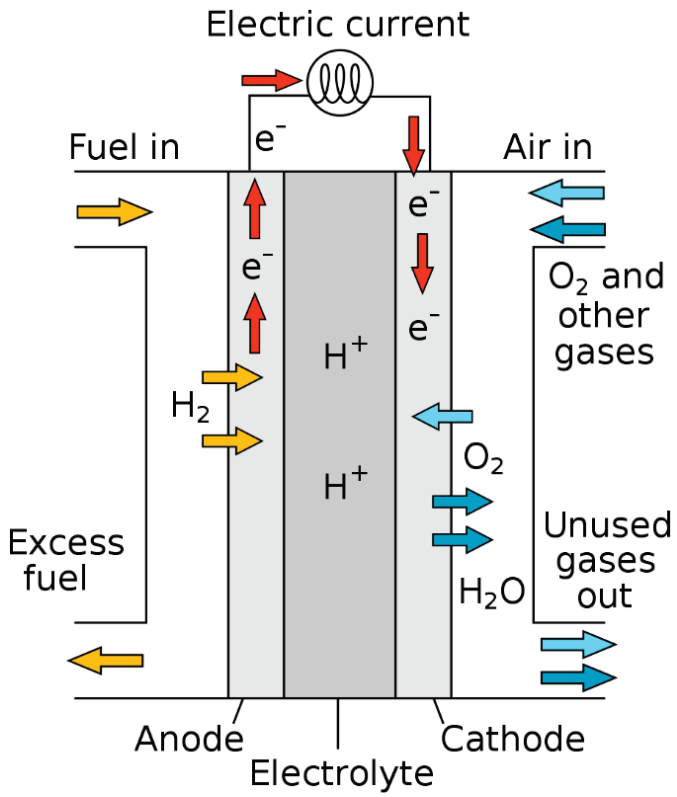

Figure 2: Schematic representation of proton-exchange membrane fuel cell.[8]

Fuel cells can be categorized according to the choice of electrolyte, such as alkaline fuel cells (AFC), proton exchange membrane fuel cells (PEMFC), phosphoric acid fuel cells (PAFC), molten carbonate fuel cells (MCFC), and solid oxide fuel cells (SOFC). AFCs, for example, use aqueous solution of KOH as the electrolyte and operate at relatively low temperatures between 20 °C and 80 °C. In contrast, PEMFCs, whose operation ranges from -40°C to 90°C, have hydrogen ions as mobile cations, with either air or oxygen serving as oxidants. Different types of fuel cells are suitable for specific applications. For example, PAFCs and MCFCs are more suitable for power plants because of their high power output. PEMFCs are becoming increasingly important, especially in automotive and stationary applications, due to their rapid start-up, flexible operating temperature (-40 to 90°C), and high energy specificity. Water and thermal management remain a key challenge for PEMFCs. The main characteristics of different types of fuel cells are shown in **Table 1**.[4,5,6] Throughout the lab course, the focus will be on the ORR electrocatalysts for PEMFC applications.

Table 1: Classification of main fuel cell properties.[4]

Type	AFCs	PEMFCs	PAFCs	MCFCs	SOFCs
Electrolyte	KOH	Perfluorosulfonic acid ionic exchange membrane	H_3PO_4	$Li_2\ CO_3$-K_2CO_3	Yttria-stabilized zirconia (Y_2O_3–ZrO_2)
Conductible ions	OH^-	H^+	H^+	CO^{2-}	O^{2-}
Fuel	H_2	H_2, CH_3OH	Reformed fuel (CH_4, CO, H_2)	Purified coal gas, natural gas, and reformed fuel (CH_4, CO, H_2)	Purified coal gas and natural gas (CH_4, CO)
Oxidant	O_2	Air	Air	Air	Air
Catalyst	Pt/Ru	Pt/Ru	Pt	NiO	Ni
Operating temperature	65 – 220 °C	−40 – 90 °C	150 – 200 °C	650 – 700 °C	600 – 1000 °C
Theoretical voltage	1.18 V	1.18 V	1.00 V	1.12 V	1.13 V
System efficiency	60% – 70%	43% – 68%	40% – 55%	55% – 65%	55% – 65%
Application	Special ground and aerospace°	Electric vehicle, submarine, and mobile power source	Regional power supply (e.g., power plant)	Power station	Power station
Development	Rapid development at 1–100 kW	Rapid development at 1–300 kW with high cost	Rapid development at 1–200 kW with high cost	Mainly development at 250–2000 kW with short life	Mainly development at 1–200 kW with high preparation technology cost

PEMFCs

The PEFC features fast start-up and low-temperature functionality. Hydrogen-fueled PEFCs are preferred for various energy applications due to their high power density, efficiency, and adaptability to different temperatures. PEFCs feature high energy density, scalable modular design, and quiet, vibration-free operation suitable for both stationary and vehicle operation.[9] The chemical reactions occur at the interface between the electrode and the electrolyte, forming a three-phase barrier that generates electrons and ions. For broader applications, such as electric vehicles or power plants, the power density of fuel cells can be optimized by increasing the active electrode surface area and stacking cells.[10]

The membrane electrode assembly (MEA) is a central component in PEMFCs and consists of three layers: the membrane, the gas diffusion layer (GDL), and the catalyst layer (CL). This structure, shown in **Figure 3**, facilitates mass transfer and accommodates electrochemical reactions, thus determining the efficiency, durability, and cost of PEMFCs.

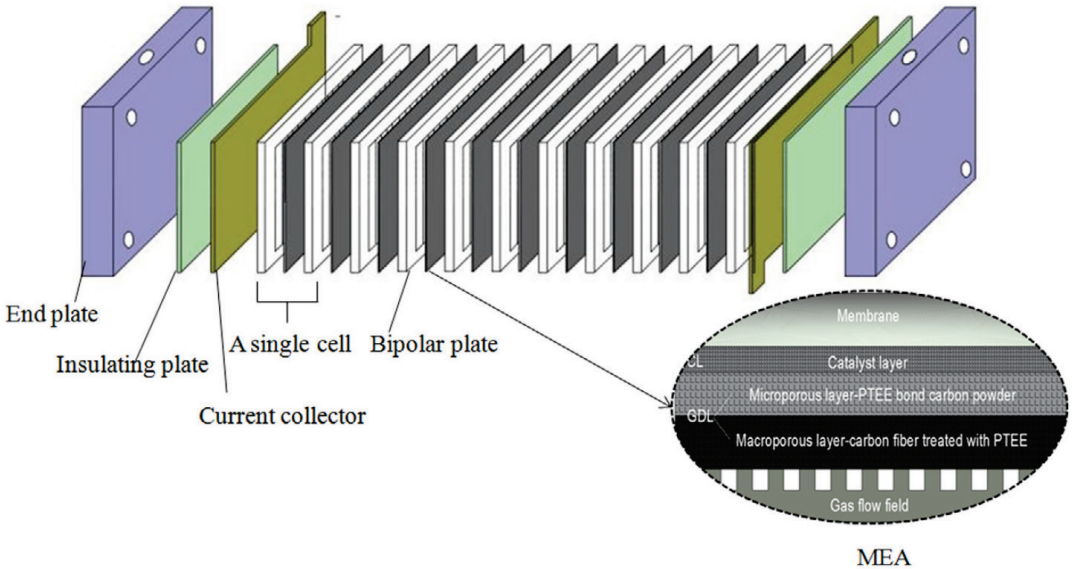

Figure 3: Basic structure of typical staking PEMFCs.[4]

The GDL, which is composed of carbon and other hydrophobic materials, such as polytetrafluoroethylene (PTFE), creates pathways for gases and electrons. It not only serves as a support structure for the CL but also provides electron conduction. PTFE is particularly important because it supports gas and water movement, especially under conditions in which flooding can occur. In contrast, the CL is where the chemical reactions occur, converting hydrogen and oxygen into water and electricity. The preparation process of the GDE, although simple, is challenging. It involves coating a CL onto a GDL to create a PEM, which is then hot-pressed to form the MEA. However, this method makes it difficult to precisely control the catalyst, resulting in suboptimal catalyst utilization (less than 20%) and higher costs.[4]

Next, PEFCs use a polymer electrolyte based on perfluorosulfonic acid ionomer (Nafion®) that serves as a thin membrane. This design reduces resistance, allows efficient proton transport, and acts as a physical and electrical barrier between the anode and cathode. The efficiency of a PEMFC is directly affected by the power output of the PEM. Ideally, a PEM should have high proton conductivity, proper water content and gas permeability, and solid electrochemical and mechanical stability.[4]

However, the transition to a fuel cell-powered world is not without challenges, such as high cost and limited durability.[11] For PEMFCs to function optimally and last a long time, strict heat and water management is essential. Issues such as catalyst area flooding and flow field channel problems can affect performance. Proper hydration of the membrane is necessary for better ionic conductivity, but excessive humidity can lead to cathode flooding. An optimal balance between membrane dehydration and hydration is critical.[12]

Furthermore, not all the chemical energy converted to electrical energy can be used. This is due to the activation (reaction kinetics), concentration (transport of reactants), and ohmic (cell components and interconnect resistance) overpotentials, as shown in **Figure 4**.[13,14]

Active, selective, and stable electrocatalysts are needed to overcome the activation overpotential and develop efficient FC.

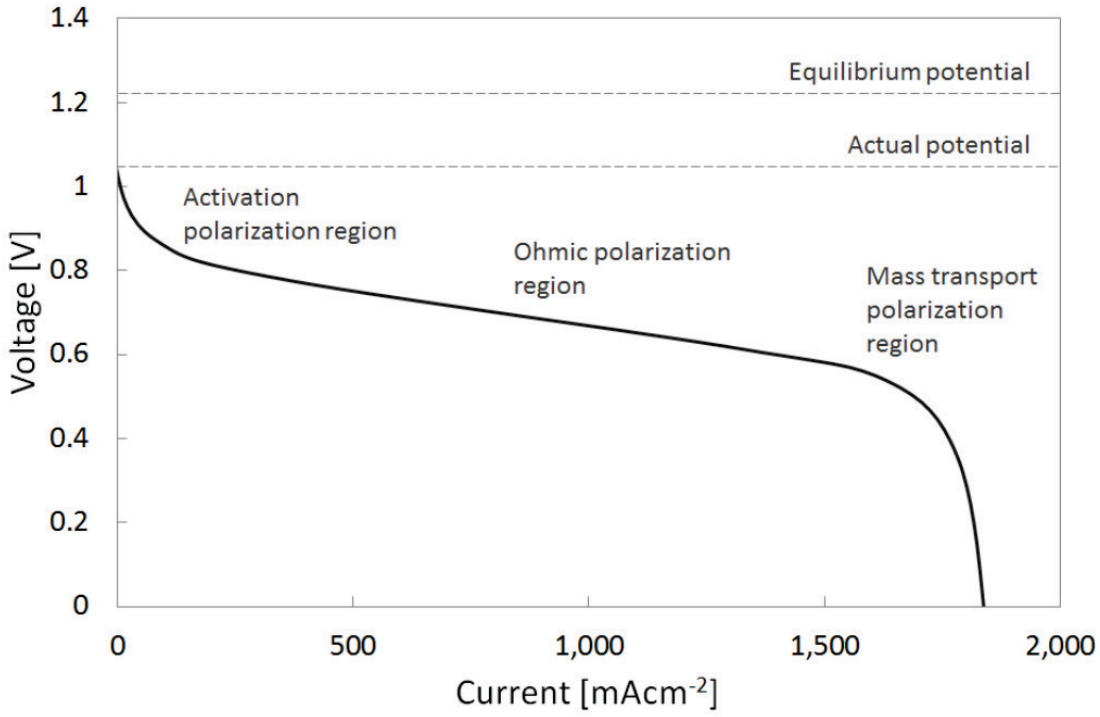

Figure 4: Typical polarization curve of the FC.[15]

For the PEMFC to truly become a cornerstone in the fight against global warming, several hurdles must be overcome. These include the production of green hydrogen and the development of durable, cost-efficient electrocatalysts, membranes, and graphite bipolar plates.

Electrocatalyst

The major cost factors in PEFC development are the electrocatalysts, which are often platinum (Pt) on a carbon support, raising issues of material cost (36–56% of total PEMFC cost)[16,17] and durability. Pt is the preferred catalyst due to its high corrosion resistance and work function, and it is used for both anode and cathode. However, the kinetics of oxygen reduction (ORR) on the cathode side is a bottleneck of the fuel cell system. The kinetics of cathode compared to anode reaction is ~5 times slower. This fact means that the cathode should contain 80~90% of the total Pt of the stack; therefore, the selection of an optimal cathode catalyst for increasing the efficiency of PEMFC is critical.[6]

Despite the inertness of Pt, it has been shown there is a decrease in cathode kinetics over time, especially due to the degradation of Pt on carbon support. This degradation affects the efficiency of the fuel cell. Various Pt-on-C degradation routes, such as Pt dissolution, Ostwald ripening, agglomeration, particle detachment, and carbon corrosion, are presented in **Figure 5**. In addition, properties such as the degree of oxide coverage of the Pt change with varying cathode potential affect fuel cell efficiency. [1,18,19]

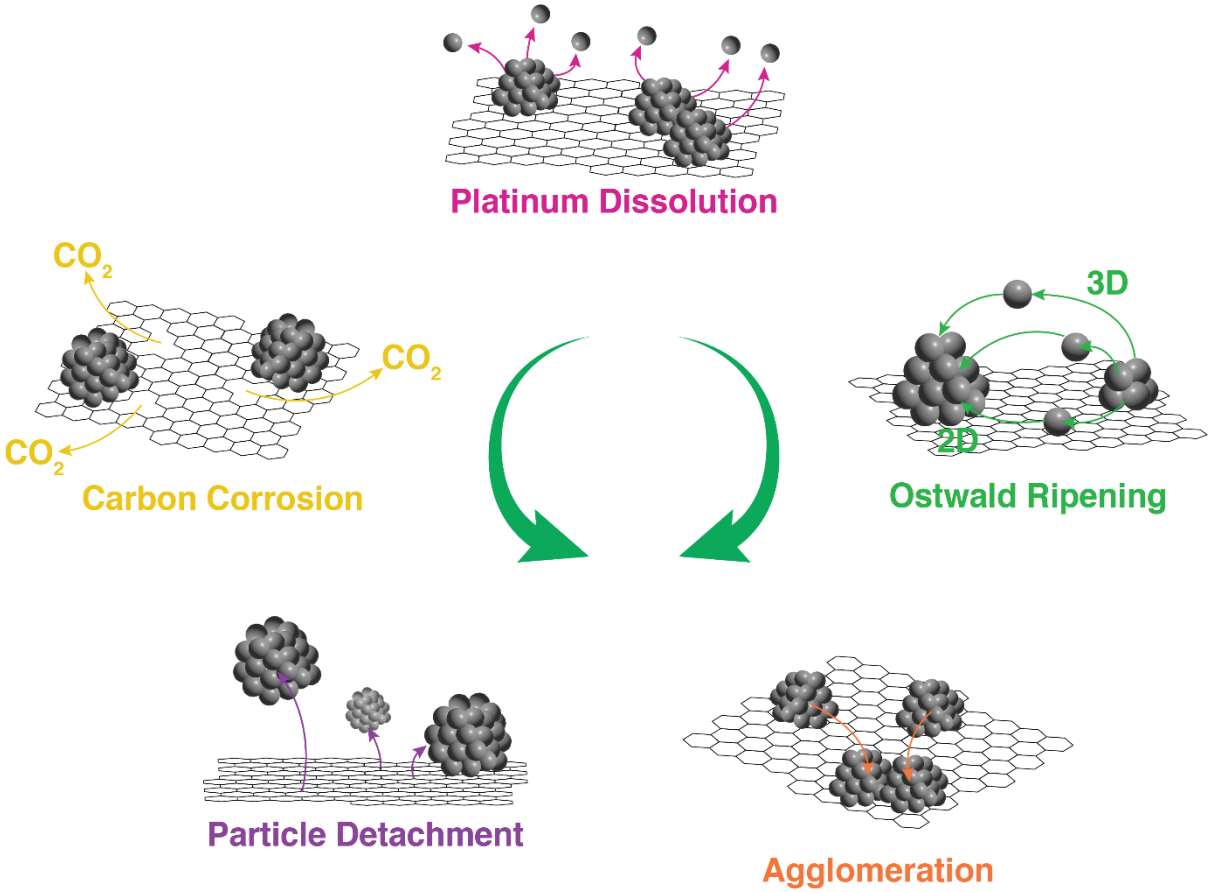

Figure 5: Degradation paths for Pt on carbon-based electrocatalysts.

Platinum-carbon-based catalysts, however, have been the focus of research, with most studies concentrating on reducing cost and increasing electrocatalytic performance.[20] Among the most promising methods, the use of Pt nanoparticles, Pt alloys combining Pt with transition metals such as cobalt (Co), copper (Cu), nickel (Ni), or iron (Fe) also further increased ORR activity.[2122] For example, Pt_3Co Pt_3Ni[23,24] and $PtCu_3$[25] have shown increased ORR activity compared to pure Pt.[22,23] Another method that consumes less Pt and maximizes Pt surface area is the preparation of core-shell catalysts. These catalysts are composed of core material (often a cheaper metal) deposited to carbon support covered by a thin Pt shell. Materials to boost the stability of support have also been developed. Among them, modified carbon-based catalyst supports with high graphite content have been shown to be advantageous, such structures based on graphene derivatives.[26]

To further decrease the cost of ORR electrocatalyst, Pt was replaced with transition metals. The most promising material in this group is the metal-nitrogen-carbon catalyst (M-N-C), in which transition metals are coordinated with nitrogen in a carbon matrix. Examples include iron-nitrogen-carbon (Fe-N-C) or cobalt-nitrogen-carbon (Co-N-C) catalysts.[4]

To reduce the cost of ORR electrocatalysts further, the development of completely metal-free catalysts based on carbon has been established. Materials such as graphene-based materials (**Figure 6**) have been explored as potential ORR catalysts. Often, these materials are doped or combined with other elements (boron, nitrogen, oxygen, fluorine, sulfur, etc.) to enhance their catalytic activity. Among them, N-doped graphene derivatives are shown to be particularly promising. Their unique electronic structure, resulting from the synergy between the inherent conductivity of graphene and the electron-rich properties induced by nitrogen doping, offers enhanced ORR activity. In addition, its large surface area, tunable porosity, and structural robustness make it exceptionally resilient under fuel cell operating conditions.[1,18,19,27]

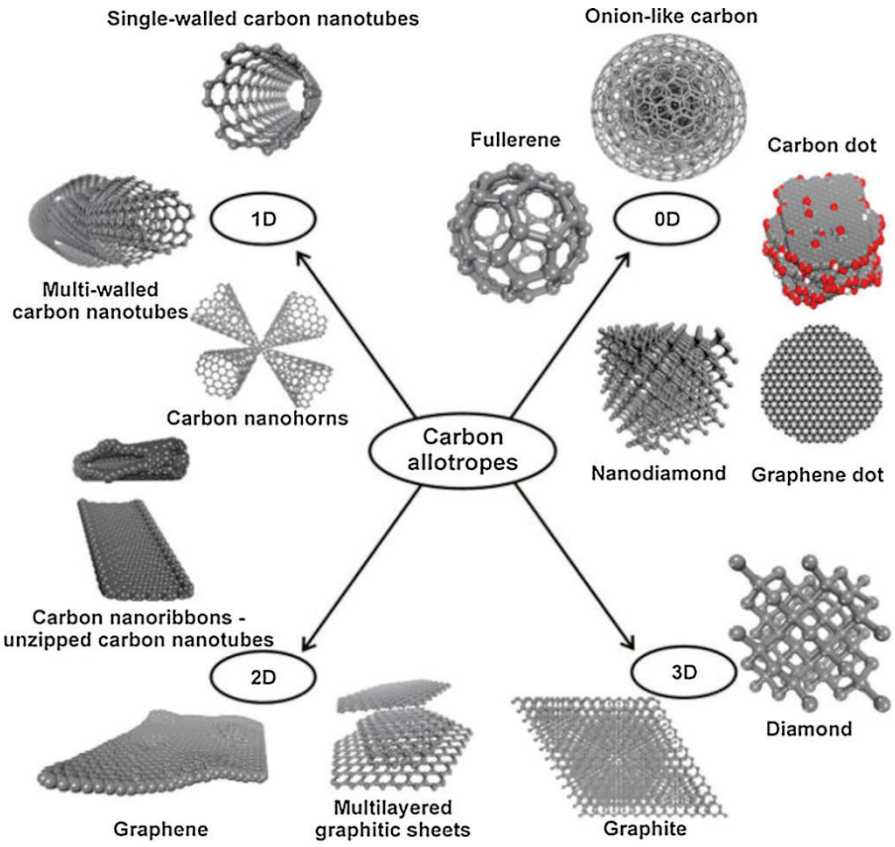

Figure 6: Carbon allotropes divided by the dimensions of the nanostructure.[28]

Nevertheless, highly crystalline graphene surfaces appear to be poor ORR electrocatalysts.[29] However, when infinite graphene sheets become finite, they exhibit different properties as the ratio of edge-to-base carbons starts to increase. The edges are more reactive due to insufficient coordination numbers.[30,31] Moreover, nitrogen doping (N-doping) of carbon nanomaterials has been proposed to further enhance the ORR activity.[32]

The experimental part of the lecture 'Carbon Materials for Energy Storage and Conversion' is divided into three parts. The first part consists of different types of synthesis; the second part consists of electrochemical characterization; the last part consists of structural, chemical, and physical characterization of graphene derivatives.

1. Synthesis of graphene derivatives

A few single-layer graphene nanosheets were first isolated in 2004 by mechanically exfoliating highly oriented pyrolyzed graphite with adhesive tape.[33] Although this type of exfoliation is preferred for a detailed study of the structural properties of graphene, the method is not appropriate for large-scale graphene production. Among the many graphene synthesis methods shown in article[34] (**Fig 1 a-e**), the syntheses are divided into **top-down** (chemical, solution-based, mechanical, and electrochemical exfoliation) and **bottom-up** (organic synthesis, CVD, epitaxial growth). The most common approach for large-scale production of graphene oxide and graphene oxide nanoribbons is chemical graphite exfoliation or unzipping of multi-walled carbon nanotubes using strong oxidizing agents, resulting in a non-conducting hydrophilic graphene oxide (GO) or graphene oxide nanoribbons (GONR).[35]

1.1. Synthesis of graphene derivatives with an improved Hummers method

The first synthesis will be the improved Hummers synthesis. The method has been optimized to produce GO with the highest oxygen content. In addition, the synthesis does not contain $NaNO_3$, and no toxic NO_x gases are produced. Simply put, in the first step of the improved Hummers synthesis, the oxidant moves between the graphite layers and oxidizes the carbon to form functional groups such as epoxides, alcohols, ketones, carbonyls, and carboxyl groups. In the second step, the layers are separated by centrifugation, ultrasonication, or thermal expansion, producing GO or GONR products.[36]

Chemicals: Graphite (Imerys, Timrex KS6L and KS44), H_3PO_4 (Sigma-Aldrich, ACS reagent, ≥ 85 wt.% in H_2O), H_2SO_4 (Sigma-Aldrich, ACS reagent, 95.0 – 98.0 wt.%), HCl (Sigma-Aldrich, ACS reagent, 37 wt.%), $KMnO_4$ (Sigma-Aldrich, ACS reagent, ≥ 99.0 wt.%), H_2O_2 (Sigma-Aldrich, ACS reagent, 30 wt.% in H_2O).

Procedure: (*Note that the synthesis contains highly concentrated acid and strong oxidizing agents; additional safety equipment is required*).

Add 100 mL of concentrated H_3PO_4 to a 5 L beaker. Set the Teflon stirrer and set the rotation speed to 300 rpm. Next, slowly add concentrated H_2SO_4 until the H_2SO_4/H_3PO_4 ratio (V:V = 9:1) is reached (always add the denser solution to the less dense one). Following that, slowly add 20 g of graphite (Imerys, Timrex KS6L or KS44). Allow the solution to cool, and after stirring (**very slowly**) for 6 hours, add 20 g of $KMnO_4$ to the mixture. An aliquot of 20 g $KMnO_4$ should be added on the 1st, 2nd, 3rd, 4th, and 5th days after the first addition of $KMnO_4$ (for a total of 6 aliquots of 20 g $KMnO_4$ on 6 different days). The reaction mixture should be left under constant stirring. One day after the last addition, the reaction mixture is poured on ice (about 800 mL), and 30 vol.% H_2O_2 is added dropwise until the color changes to yellow.

The mixture is then centrifuged in plastic tubes at 4100 rpm for 30 minutes (Note: The centrifuge tubes should be balanced according to their weight in the centrifuge rotator, and the outside of the tubes should also be wiped with paper towels). The supernatant is decanted, and the remaining solid is washed with H_2O and centrifuged again at 4100 rpm for 30 minutes. After the supernatant is removed, the remaining material is washed again and centrifuged successively with 10 wt.% HCl and H_2O at 4100 rpm for 90 minutes. After this multiple washing, the remaining material is freeze-dried and stored at room temperature.[37]

Questions

1. What types of overpotentials occur in FC devices? How is overpotential defined? Why are low overpotentials desirable for FC devices?

2. What two processes are responsible for the potential drop from reverse to the potential at the OCP (see **Figure 4**)?

3. What is the strongest oxidizing species in the Hummers reaction responsible for the oxidation of carbon nanostructures? Provide a reaction equation.

4. Why should we always pour a denser solution into a less dense solution?

5. What are the main differences between top-down and bottom-up synthesis approaches?

1.2. Synthesis of graphene derivatives with induction and convection heating

The first report of N-doped graphene used as an efficient electrocatalyst for ORR was synthesized by the CVD method in 2010.[38] Since then, many experimental and theoretical studies followed to explain the positive effects of N-doped carbon nanostructure on ORR.[39,38] The results of density functional theories[40,39] showed that N-doping shifts the Fermi level of the carbon nanostructure, which makes the graphene material behave like a semiconductor and changes the charge density and spin density of the carbon atoms near the N-doped atoms. The N-doping induces what is known as an "activation region" on the surface of the graphene lattice. It is speculated that this type of activated region accelerates the rated limiting step (usually oxygen adsorption from the electrolyte/gas on the carbon nanostructure) in ORR.[40,39]

In general, N-doped graphene derivatives can be prepared with two different methods: with direct synthesis (CVD, segregation growth, solvothermal, arc discharge, etc.) and post-treatment (thermal treatment with various N precursors, N_2 plasma treatment, N_2H_4 reduction) of undoped graphene derivatives. The main difference between the methods is the type of doping. In post-treatment, homogeneous doping occurs at the surface, while in direct synthesis, it also occurs in the bulk of the carbon nanostructure. Another difference between the methods is the concentration and configuration of N-doping in the carbon nanostructure. However, these are not easy to compare because different reaction processes and conditions are used for their synthesis.[41]

In this exercise, we will prepare N-doped heat-treated graphene oxide and N-doped heat-treated graphene oxide nanoribbons from previously prepared GO and GONR by heating in a furnace and by induction. The difference between the two heating methods is that the furnace uses Joule heating; in contrast, for induction heating, we first generate an alternating magnetic field through a Cu coil (as can be seen in **Figure 7**). This alternating magnetic field then induces electric currents in the conductive material (graphite holder) and, similar to the furnace, heat is generated by the resistance of the material. Another advantage of induction heating is the faster heating rate of 100 °C/s, compared to furnaces or autoclaves at 100 °C/min.[42]

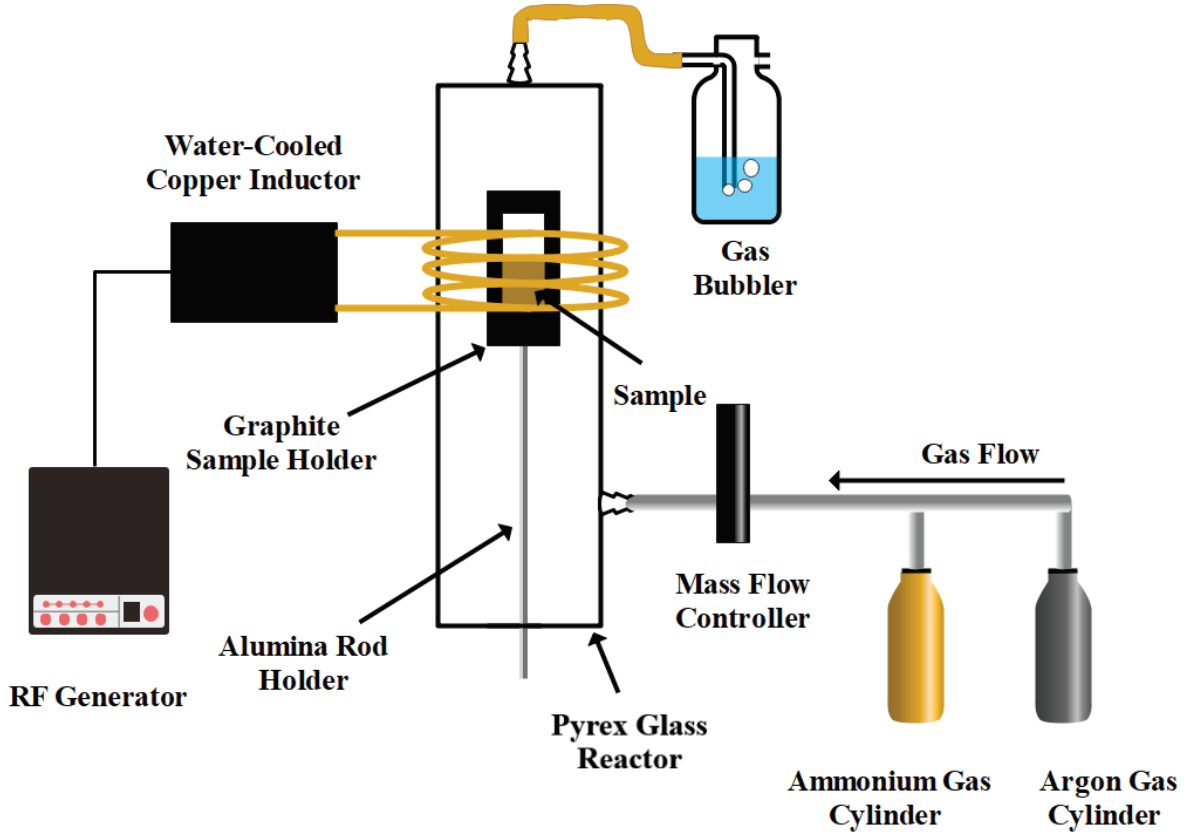

Figure 7: Scheme of RF-assisted heat-treating synthesis system.

1.2.1. Convection heating

Weigh approximately 0.5 g of the GO or GONR sample prepared with the improved Hummers method into a crucible containing alumina (Al_2O_3). Place the alumina crucible with the sample in the quartz tube in the center of the split tube furnace. Close the furnace and connect the quartz tube to the inlet of the NH_3 gas. Set the NH_3 gas regulator to a flow rate of 150 mL/min. Set the parameters of the furnace as follows: heating rate 10 K/min from room temperature to 800 °C, hold the temperature at 800 °C for 1 minute, turn off the heating, and wait for the furnace to cool down.

Note: The flow regulator used for the reaction is calibrated for H_2. Using the following equation $f_{NH3} = f_{H2} \cdot \sqrt{\rho_{H2}/\rho_{NH3}}$, calculate the correct flow rate for the NH_3 gas, where f is the volumetric flow rate, and ρ is the gas density at standard conditions.

1.2.2. Induction heating

Weigh about 170 mg of the sample GO or GONR prepared with the improved Hummers method into a graphite crucible. Cover the top of the graphite crucible and place it on the alumina rod in the quartz tube in the center of the Cu coil. Cap the quartz tube and set the NH_3 gas regulator to a flow rate of 150 mL/min. Turn on the Cu coil cooler and then the inductor.

Set the current to 52% A (390 A) and press the start button on the inductor (during the operation, do not touch the instruments). Observe the temperature of the graphite pot until it reaches 800 °C. Then, switch off the inductor and the Cu coil cooler.

Questions

1. What are the main advantages and disadvantages of furnace and induction heating?

2. How does the increase in frequency influence the induction heating of conducting samples?

3. Was the graphene derivative in the graphite holder also affected by the magnetic field generated by induction?

4. What device was used to monitor the temperature during induction heating? What material property does it measure?

5. What is meant by a “perfect emitter”? Emissivity is a function of what parameters?

1.3. Preparation of graphene derivatives with Flash Joule heating

Despite the countless potential applications offered by graphene properties, efficient and cost-effective mass production remains a hurdle. As an answer to that, Flash Joule Heating (FJH) emerged in 2020 as an innovative technique capable of synthesizing graphene on a gram scale from a variety of carbon-based materials, including carbon black, metallurgical coke, and even discarded plastics.[4344]

The FJH method utilizes intense Joule heating induced by the passage of a high electrical current, leading to structural changes in the carbon material. The extraordinarily high temperatures of over 3000 K facilitate the breaking of molecular bonds, allowing the carbon atoms to reorganize into a stable sp^2-hybridized graphene structure.[45] As the cooling of the overheated carbon material takes place within fractions of a second, the graphene sheets produced are trapped in a turbostratic non-equilibrium state, uniquely termed "flash graphene" (FG). The "non-equilibrium" conformation means a less energetically favorable arrangement compared to the ideal AB stacking seen in standard graphite. In contrast to conventional graphite, in which the carbon layers line up in the ordered Bernal stacking (ABAB... sequence), turbostratic graphene is characterized by its disordered layer arrangement. This disorder allows the layers to rotate independently of each other and to assume any angle to each other. Such misalignment results in the layers not being regularly stacked but lying on top of each other randomly and without specific orientation.[46]

The resulting turbostratic configuration gives the material unique properties. Such as, **increased reactivity** (the misaligned layers may expose more edge sites and defects that are more chemically reactive), **improved solubility (**disorder between the layers reduces the van der Waals forces that hold the layers together, making turbostratic graphene easier to disperse), **electrical properties** (disorder can lead to improved electrical properties by creating more pathways for charge carriers), **flexibility in composites** (the layers can slide over each other more easily).[47]

To increase electrocatalytic efficiency, the induction of intrinsic defects, such as vacancies, Stone-Wales transformations, line defects, and edge dislocations, is crucial. These defects, whether in the basal plane or along the periphery of the carbon lattice, disrupt the π-conjugation system. The introduction of these perturbations alters the electronic properties of neighboring carbon atoms, leading to a change in polarization that allows new active sites for catalytic reactions, which are essential for the overall performance of electrocatalysts.[48,49]
The FJH approach is remarkable not only for the unique turbostratic structure but also for the fast processing time, environmental sustainability, and exceptionally high quality of the graphene sheets that are produced. Its ability to convert waste materials into a high-quality product underlines its role in promoting the circular economy and promises to renew the commercial production of graphene. Currently, FJH is reported to be one of the cheapest and

fastest ways of producing graphene. As a pioneer on the road to sustainability, FJH has the potential to become a key technology for the mass production of graphene. If research continues to progress, FJH could become a cornerstone technology for the mass production of graphene and have a profound impact on energy technologies and sustainability initiatives.[46]

Procedure:

The following procedure is used for the preparation of the sample for FJH: The Ketjenblack (KB, a type of carbon black) used comes in the form of pellets, which must be ground. For this purpose, Milli-Q water is added to about 5 g of KB and placed on a magnetic stirrer with a heater until a thick, homogeneous mass is obtained. Metal precursor salt dissolved in Milli-Q water is added to it. The sample is heated until the water evaporates, and a homogeneous mixture of KB and the metal salt is left. In the final stages of drying, the mixture is moved to a laboratory dryer and periodically stirred. In this way, almost all the contained water is evaporated. The procedure is presented in **Figure 8**.

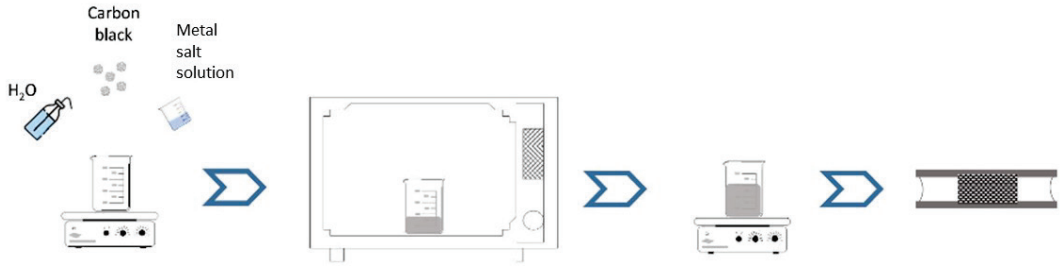

Figure 8: Schematic representation for preparation of homogeneously dispersed metal particles on KB.

The FJH system is powered directly from the power network using a half-wave rectifier. The electrical current passing through the sample is delivered by a capacitor bank. It is made of 12 parallel-connected capacitors with a total capacity of 72 mF, and a maximum operating voltage of 400 V. A thyristor switch controlled by an Arduino microcontroller is used. When a signal is supplied from the microcontroller, thyristor 1 is opened, and the capacitor bank is discharged sequentially through resistor 1 (R_1), resistor 2 (R_2), and the sample (**Figure 9**) in which the sample of carbon material is placed. When the preset discharge time is reached, the Arduino microcontroller provides a tripping signal to thyristor 2, which provides an alternative circuit with less resistance for the current coming from the capacitor bank. In this way, the current through the sample decreases practically to 0, the capacitor bank quickly discharges, and the process of heating the sample ends. R_1 is used to limit load in the circuit and prevent overloading of the thyristor switch. R_2 serves both as a shunt and as an additional load, limiting the current through the sample after thyristor 2 is opened.

A digital oscilloscope connected to a personal computer (OSC) is used to measure current and voltage. One channel of the oscilloscope is used to measure the current passing through the sample by means of the voltage drop over resistor 2. The second channel of the oscilloscope measures the voltage of the capacitor bank to determine subsequently the amount of electrical energy introduced into the sample.

The system is also equipped with a sample preheating module that uses alternating current directly from the power network. The purpose of preheating is to slowly release a maximum of moisture and gases absorbed in the sample.

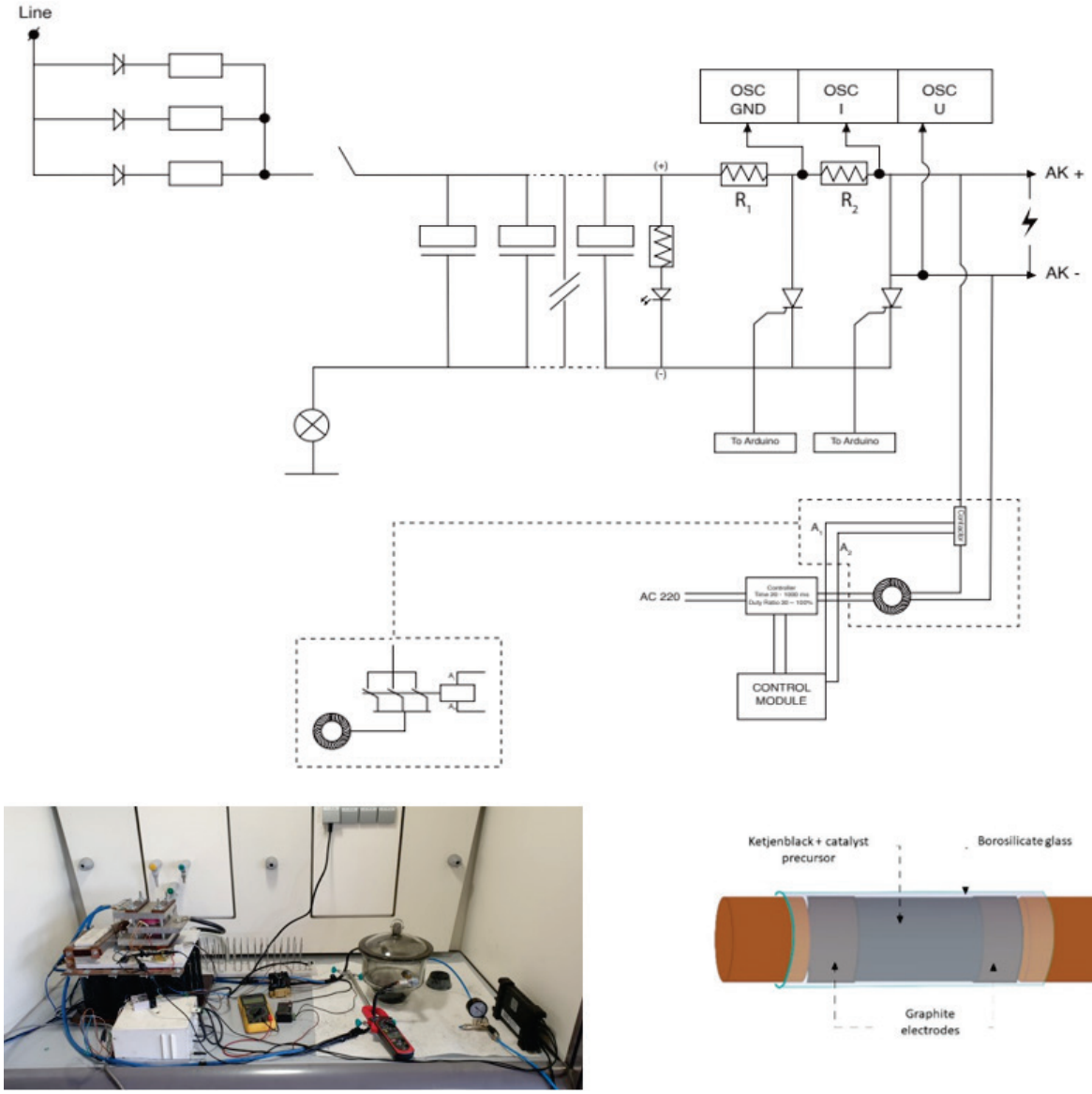

Figure 9: Scheme of FJH instrumentation.

Questions

1. Calculate the amount of energy needed to heat 50 mg of carbon from 0 °C to 3550 K (boiling temperature).

2. Calculate the amount of energy needed to sublimate 50 mg of carbon from 0 K.

3. Calculate the amount of energy stored in a 72 mF capacitor charged to 320 V. Present it in Joules.

1.4. Chemical vapor deposition.

CVD is the leading method for graphene growth. During the CVD process, chemical reactions form a thin film of vapor species on the substrates. In a typical CVD setup, as shown in **Figure 10**, to synthesize N-doped graphene, we need two C and N precursors, or a precursor containing both C and N atoms, in the presence of an inert/reducing gas carrier (N_2, Ar, Ar/H_2, etc.) and a metal substrate (Cu, Ni, Pt, Ir, etc.) heated to a temperature at which it acts as a catalyst for precursor degradation and subsequent deposition. The typical N precursors are NH_3, pyridine, polypyrrole, etc., while CH_4, ethene, etc., are usually used for the C precursors.[41] Depending on the solubility of the C atoms in the heated metal substrate, there are two mechanisms for graphene growth. If the solubility of the C atoms in the metal is high (e.g., Ni), graphene growth follows segregation as the metal cools. However, if the solubility of the C atoms is low (e.g., Cu), direct decomposition and adsorption occur. After the growth of graphene on the metal surface, the N atoms are incorporated into the graphene lattice as a substitute.[41]

By changing the CVD synthesis parameters, system design, reactor configuration, gas feed material, gas ratios, reactor pressure and gas partial pressures, reaction temperature, growth time, temperature, etc., we can influence the content and type of N.[41,50,51]

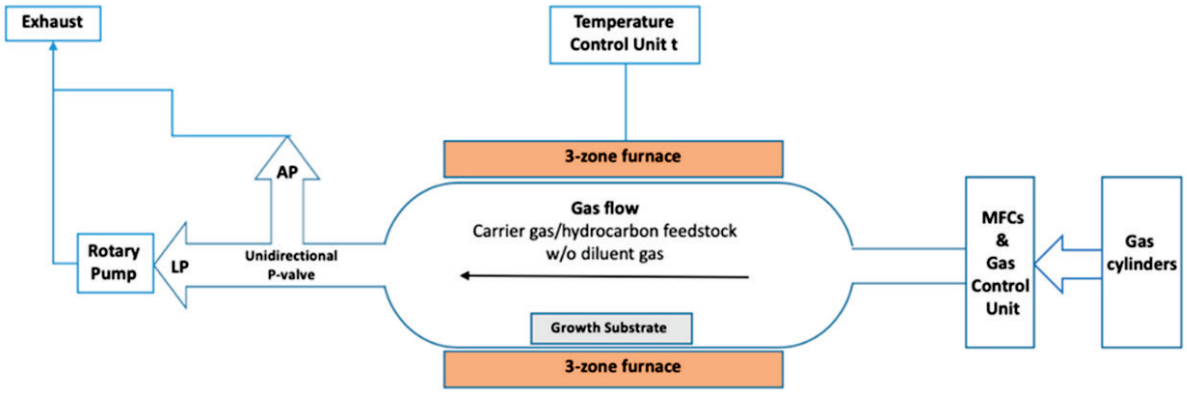

Figure 10: Schematic diagram of a typical hot-wall horizontal tube-furnace CVD system (LP: low pressure, AP: atmospheric pressure).[51]

Preparation of metal substrate (Cu, Ni)

Before the electrochemical measurement, we perform a mechanical polishing of the electrode. During mechanical polishing, we remove all scratches, gouges, and other damages on the surface. Also, the surface should be as smooth as possible for deposition to avoid unnecessary defects in the graphene structure. We start with the largest particle size of the alumina powder (1 µm). We apply half a teaspoon of alumina powder on the polishing layer and mix it with Milli-Q water to produce a polishing paste. Then, we take a Cu or Ni electrode and carefully press it vertically onto the surface. To achieve the most homogeneous polishing, the latter

should be done in the form of the numeral 8 with a constant force applied parallel to the surface of the polishing layer. After polishing, the electrode is rinsed with Milli-Q water and placed in an ultrasonic bath for 15 seconds. The process is then repeated with the 0.5 μm and 0.03 μm alumina powder particles.

CVD graphene growth on Cu and Ni metal substrate

Place the Cu or Ni metal substrate on an alumina crucible and slide it into the quartz tube. Next, center the Cu induction coil around the metal substrate. Next, anneal the metal surface at 1000 °C for 15 minutes and then perform graphene synthesis with NH_3, CH_4, Ar/H_2 (V:V = 96:4), and H_2 at 15, 5, 1500, and 25 cm^3/min gas flow. After 5 minutes, turn off the induction heating.

Questions

1. Why is the solubility of carbon higher in Ni than in Cu?

2. Why is the inert or reducing inert atmosphere used for CVD?

3. Why is the metal annealing step performed?

4. Is rapid graphene nucleation desirable for high-quality single-layer graphene formation? What are the parameters that affect the nucleation of reduced graphene?

2. Electrochemical characterization of electrocatalysts

Three important factors must be optimized for the development of an efficient electrocatalyst: activity, selectivity, and stability. Activity is directly related to the exposed active sites on the catalyst and is a key factor in rational catalyst design. The activity of a solid electrocatalyst is determined by intrinsic parameters (active sites) and extrinsic parameters (exposed active sites) at a given mass loading. In the non-metallic carbon nanostructures, the activity is further enhanced or decreased by the introduction of porosity, defects, and irregularities in the structure, i.e., more edges and doping. Selectivity, in turn, affects how much of the current during the reaction is used to produce the wanted product or how much is lost to parasitic side reactions. With the stability, we investigate the durability (operating time under certain conditions) of the electrocatalyst.[52]

In the second part, we will present two commonly used electrochemical methods, RDE and RRDE, and the corresponding protocols for activity, selectivity, and stability measurements on previously prepared graphene derivatives, Pt/C and Ni/C.

2.1. Rotating disk electrode (RDE)

During the electrochemical reaction at the electrode and in its vicinity, many processes take place. In general, they can be divided into two groups: electrochemical and transport processes. The electrochemical processes are then further divided into the Faradaic (electrochemical reaction) and non-Faradaic (double layer charging, adsorption) processes and the transport processes into ion migration, diffusion, and convection. These processes can occur simultaneously, which makes it difficult to study the system.[53,54]

To eliminate one of the transport processes, the effect of ion migration, an excessive concentration of the supporting (inert) electrolyte is used. In a concentrated electrolyte system without convection, the only meaningful transport process is diffusion. Since the concentration is time-dependent according to Fick's second law **Equation (3**), and hence the thickness of the diffusion layer at the electrode surface, it is impossible to maintain a steady-state reaction rate if it is based only on reactant diffusion transport (ex).[53]

However, when additional convection occurs with the rotation of the electrode, the thickness of the convection-diffusion layer is no longer a function of time but of the speed of rotation of the electrode, resulting in a steady-state reaction rate. Note that the thickness of the convection-diffusion layer is different from the thickness of the classical diffusion layer. Here, although there is diffusion, there is also convection. Two popular techniques that use convection-diffusion processes to study electrochemical and transport properties are the rotating disk electrode (RDE) and the rotating ring disk electrode (RRDE).[54]

In **Figure 11 a),** we see a schematic diagram of the RDE. The surface of the rotating electrode disk is in contact with the electrolyte solution. Around the disk electrode, an electronic insulator (Teflon) is used to cover the remaining part of the disk so that only the disk electrode is exposed. The electrolyte flows from the bulk of the solution to the surface of the electrode and then is flushed parallel to the surface of the disk, as shown in **Figure 11 b)**. With the three coordinates shown in **Figure 11 b)**, the mathematical operation for the flow rate of the solution can be expressed as follows:[54]

$$v_{\mathrm{x}} = -0.51\omega^{3/2}\upsilon^{-1/2}x^2 \quad (1)$$

$$v_{\mathrm{r}} = 0.51\omega^{3/2}\upsilon^{-1/2}rx \quad (2)$$

Where v_x and v_r are the flow velocities of the solution in the x and r directions (cm s^{-1}), ω is the rotational velocity of the electrode (s^{-1}), υ is the kinetic viscosity of the electrolyte solution (cm^2 s^{-1}), x is the distance from the electrode surface (cm), and r is the distance from the center at of the disk in the direction parallel to the electrode surface (cm).[54]

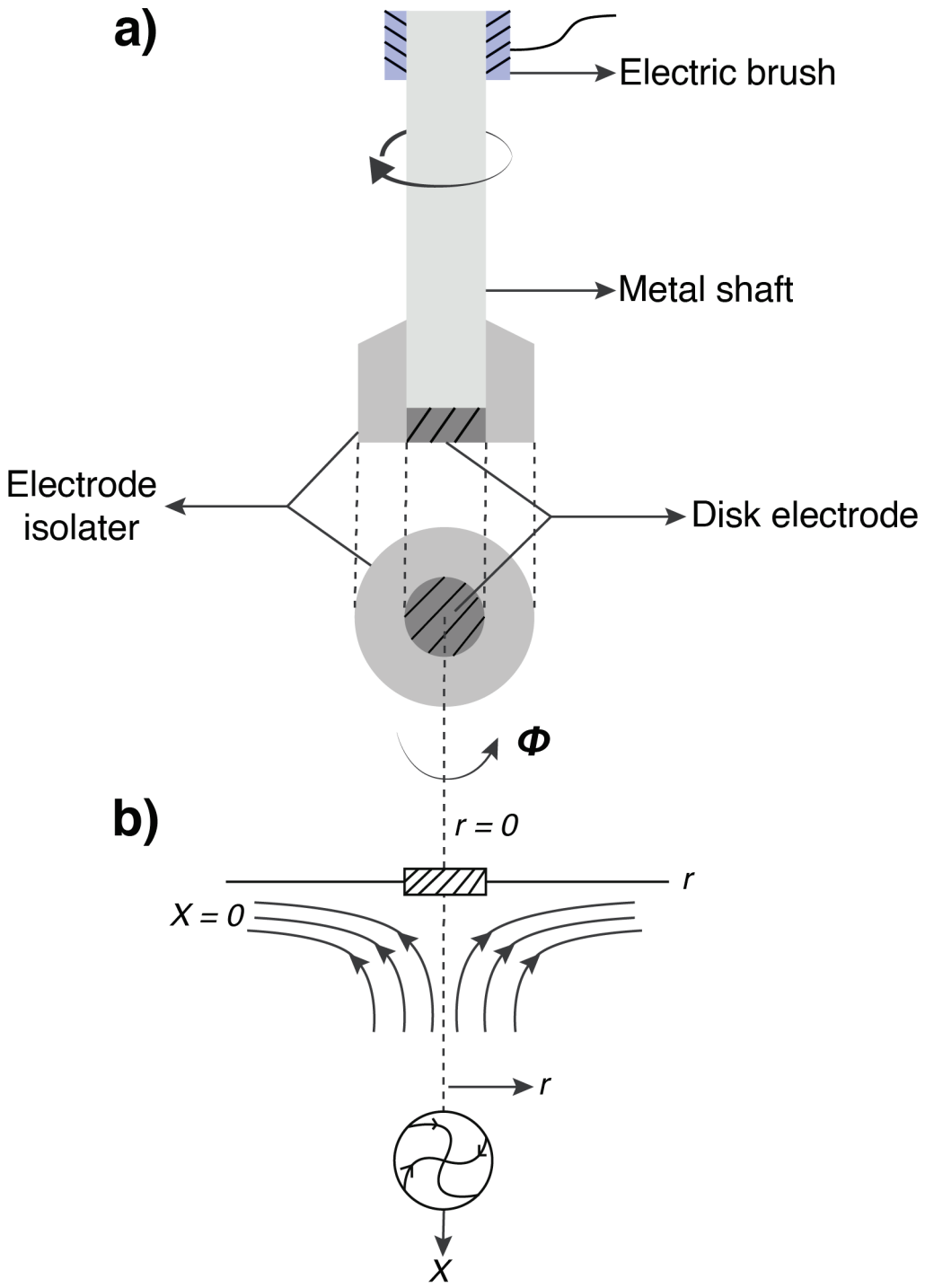

Figure 11: a) Schematic representation of the RDE parts and b) the direction of electrolyte flow near the electrode surface.

To derive the current-potential relationship for the reaction rate for RDE, Fick's second law must be used for the steady state of diffusion-convection. In a steady state, the surface concentration of the reactant reaches zero, which means that the concentration of the reactant within the diffusion-convection layer is constant. Moreover, in this condition, the convection rate and the diffusion rate are equal:[55]

$$\left(\frac{\partial C_{\mathrm{O}}}{\partial t}\right)_{\mathrm{diffusion}} = D_{\mathrm{O}}\left[\frac{\partial^2 C_{\mathrm{O}}}{\partial x^2} + \frac{\partial^2 C_{\mathrm{O}}}{\partial r^2} + \frac{1}{r}\left(\frac{\partial C_{\mathrm{O}}}{\partial r}\right) + \frac{1}{r^2}\left(\frac{\partial^2 C_{\mathrm{O}}}{\partial \phi^2}\right)\right] \quad (3)$$

$$\left(\frac{\partial C_{\mathrm{O}}}{\partial t}\right)_{\mathrm{convection}} = -\left[v_r\left(\frac{\partial C_{\mathrm{O}}}{\partial r}\right) + \frac{v_\phi}{r}\left(\frac{\partial C_{\mathrm{O}}}{\partial \phi}\right) + v_x\left(\frac{\partial C_{\mathrm{O}}}{\partial x}\right)\right] \quad (4)$$

$$\left(\frac{\partial C_{\mathrm{O}}}{\partial t}\right)_{\mathrm{diffusion}} - \left(\frac{\partial C_{\mathrm{O}}}{\partial t}\right)_{\mathrm{convection}} = 0 \quad (5)$$

Because of the location of the disc at the center, geometric symmetry shows that the oxidant concentration is not a function of ϕ or r, so: $\frac{\partial^2 C_{\mathrm{O}}}{\partial r^2} = \frac{\partial C_{\mathrm{O}}}{\partial r} = \frac{\partial C_{\mathrm{O}}}{\partial \phi} = \frac{\partial^2 C_{\mathrm{O}}}{\partial \phi^2} = 0$.
Using the above equation with the boundary conditions $C_{\mathrm{O}} = C_{\mathrm{O}}^0$ at $x = \infty$ (in the bulk solution, the concentration of the oxidant is equal to the initial concentration) and $C_{\mathrm{O}}^{\mathrm{S}} = 0$ at $x = 0$ (at the surface of the electrode, the oxidant concentration is zero), we obtain:[54]

$$\left(\frac{\partial C_{\mathrm{O}}}{\partial t}\right)_{\mathrm{x=0}} = 1.1194 C_{\mathrm{O}}^0 \left(\frac{3D_{\mathrm{O}}\omega^{-3/2}\nu^{1/2}}{0.51}\right)^{-1/3} \quad (6)$$

Finally, by combining **Equation (6)** with **Equation (7)** for limiting current density:

$$I_{\mathrm{DC,O}} = nFD_{\mathrm{O}}\left(\frac{\partial C_{\mathrm{O}}}{\partial t}\right)_{\mathrm{x=0}} \quad (7)$$

we are left with the famous Levich equation:

$$I_{\mathrm{DC,O}} = 0.62nFD_{\mathrm{O}}^{2/3}\nu^{-1/6}\omega^{1/2}C_{\mathrm{O}}^0 \quad (8)$$

Where $I_{DC,O}$ is the diffusion-convection limited current density (A cm^{-2}), n is the number of transferred electrons, and F is the Faradaic constant (96500 As mol^{-1}).[54]

In the case of fast electron transfer kinetics and a slower diffusion-convection process, the surface concentration of the oxidant quickly approaches zero. Here, we can apply Levich **Equation (9)**, in which the slope of $I_{DC,0}$ versus $\omega^{1/2}$ is a straight line with a slope of $0.62nFD_{\mathrm{O}}^{2/3}\nu^{-1/6}C_{\mathrm{O}}^0$. Using the slope n, $D_{\mathrm{O}}^{2/3}$, $\nu^{-1/6}$, or C_{O}^0 can be determined if the other three parameters are known. However, when the electron-transfer kinetics is slower than the diffusion-convection process, the surface concentration of the oxidant does not reach zero (unless very high overpotentials are used, as shown in **Figure 12**). Here, we use the following equation:[54]

$$\frac{1}{i_{\mathrm{DC,O}}} = \frac{1}{i_{\mathrm{k,O}}} + \frac{1}{I_{\mathrm{DC,O}}} \quad (9)$$

where $i_{k,O}$ is the electron-transfer current. By combining **Equations (8)** and **(9)**, we obtain the Koutecký -Levich equation:[54]

$$\frac{1}{i_{DC,O}} = \frac{1}{i_{k,O}} + \frac{\omega^{-1/2}}{0.62nFD_O^{2/3}\nu^{-1/6}C_O^0} \quad (10)$$

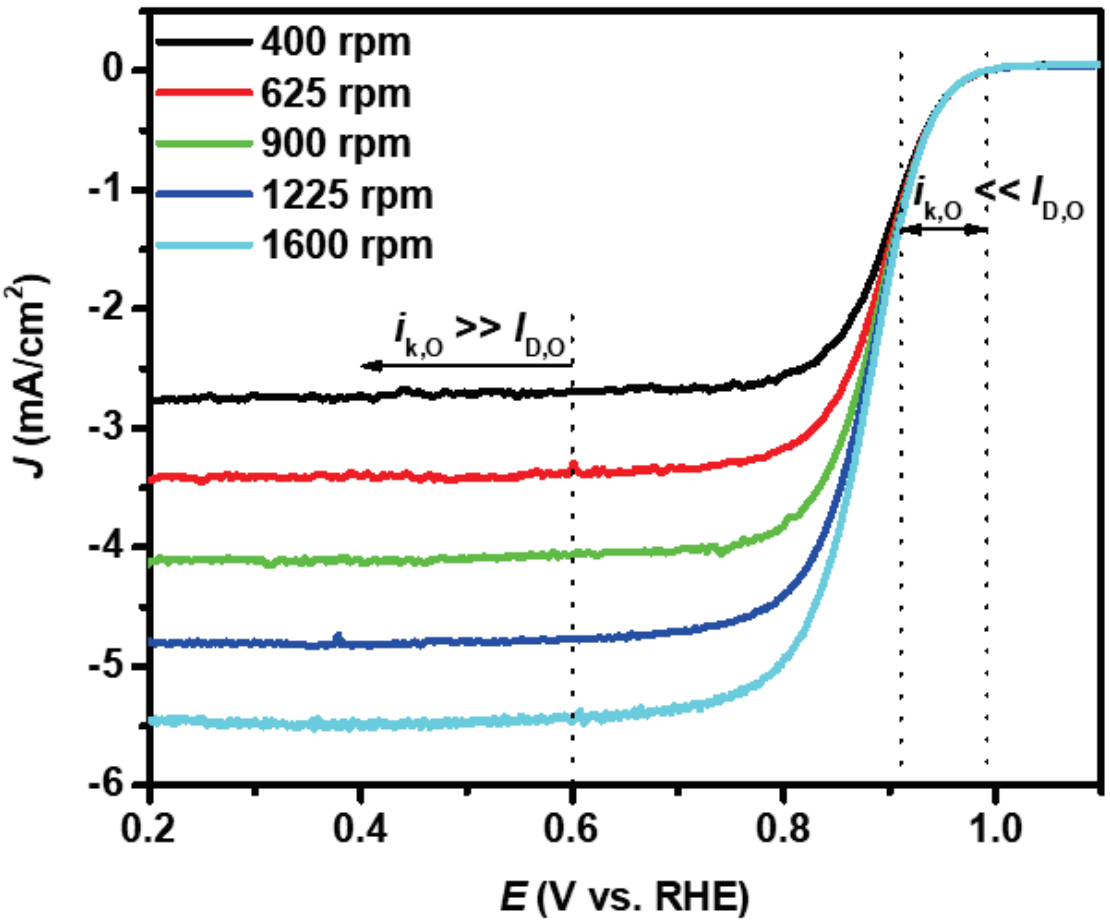

Figure 12: Polarization curves for ORR reaction on the poly-Pt electrode in 0.1 M $HClO_4$ with marked current ranges where the electron transfer (on the right side of the graph) or the diffusion process (the left side of the graph) is faster.

2.2. Rotating ring disk electrode (RRDE)

Another powerful tool for studying ORR selectivity is RRDE. The difference from RDE is that RRDE has an additional ring electrode surrounding the disk electrode. They are isolated from each other, as seen in **Figure 13**. The disk electrode and ring electrode are made of materials such as gold, platinum, or glassy carbon (GC). For this technique, we need to use a bipotentiostat because both electrodes, the ring and disk, are controlled potentiostatically at the same time. The technique is useful for the study of multi-electron processes, kinetics, adsorption, desorption steps, and electrochemical reaction mechanisms, using the ring electrode as a detector for the reaction products of the disk electrode.[55]

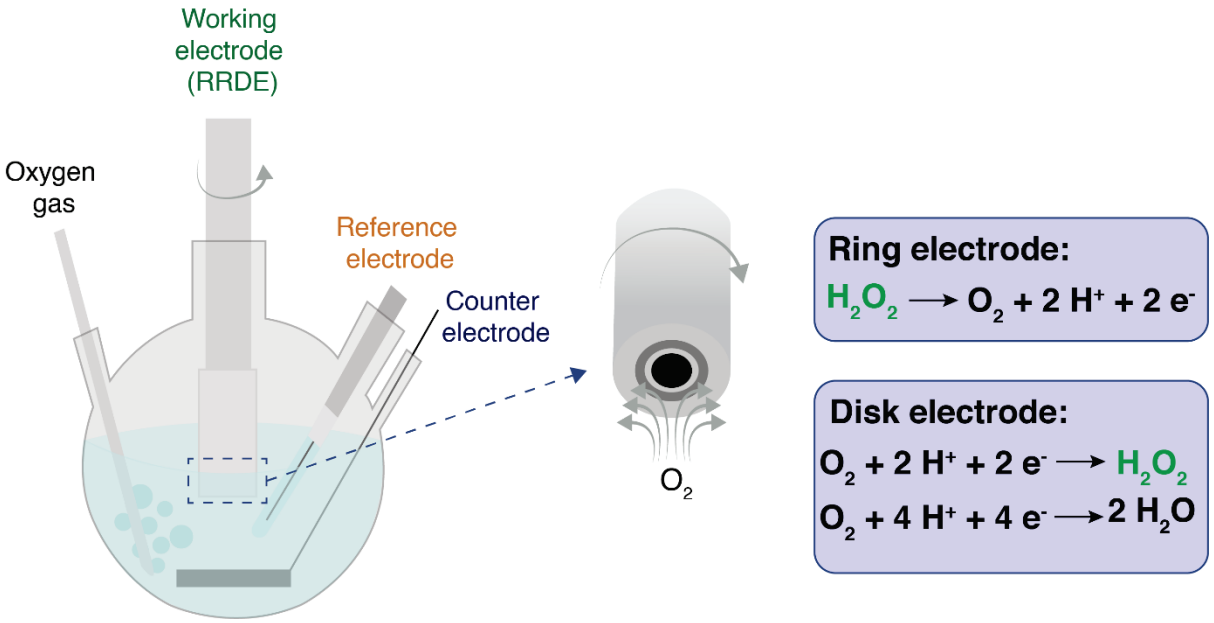

Figure 13: Scheme of RDDE, with ring and disk reactions.

Like RDE, RRDE also rotates during the measurement. If the rotation speed is sufficient, a diffusion-convection layer is formed, and the limited current density follows the Levich **Equation (8)** or Koutecký-Levich **Equation (10)**. As a result of the rotation speed of the electrode, the electrolyte flows outward from the disk electrode to the ring electrode due to centrifugal force.[55]

For example, let us look at what happens at the RRDE during the ORR experiment (as shown in **Figure 13**). At the disk electrode, the ORR takes place. Depending on the nature of the interaction of the electrocatalyst with the oxygen and the intermediates of the reaction, some peroxide may be formed. The peroxide formed then continues to flow off the surface of the disk electrode. Some of the peroxide flows into the bulk of the solution, some is decomposed, and some reaches the ring electrode. Since we want to measure the amount of peroxide formed,

the potential of the ring electrode will be constant in the region of peroxide oxidation. Therefore, all the peroxide that reaches the ring electrode will be oxidized back to water, and we will see this as a response to the ring current. Since not all of the reduced O_2 in the form of peroxide comes into contact with the ring electrode, another important parameter for quantitatively measuring peroxide formation (ORR selectivity) is the collection efficiency, which provides information on the percentage of intermediates formed at the disk electrode that comes into contact with the ring electrode.[55]

The collection efficiency depends on the rotational speed of the electrode, the diameter of the disk electrode, the outer and inner diameters of the ring electrode, the type of reaction, and the thickness and roughness of the electrocatalyst layer. Although it can be calculated theoretically from the ratio between the diameter of the disk electrode and the outer and inner diameters of the ring electrode, it is recommended to measure it experimentally from the ratio between the ring and disk currents from reversible redox reaction (ferricyanide/ferrocyanide, ferrocene, benzoquinone, hydroquinone, etc.).[55,56]

2.3. Preparation of glassware, electrode, and electrocatalyst

Before the start of electrochemical characterization, a few things need to be done. Described below are the standard protocols for preparing glassware, electrodes, and catalysts.

2.3.1. Preparation of the glassware

All glassware must be cleaned before electrochemical experiments. This is done to remove any organic or inorganic impurities (Fe, Mn, Co, Ni, etc.) that could affect the ORR activity. Since the best electrocatalysts for ORR are Pt-based, the glassware is cleaned with aqua regia, which is prepared by mixing concentrated HCl and HNO_3 acids in a 3:1 molar ratio. Care should be taken when mixing two strong acids. Despite its lower density, HCl should always be added to HNO_3 to avoid the formation of Cl_2 gas. Since aqua regia is very unstable, you should neutralize it after use and always use it freshly prepared.[57]

After washing with aqua regia, rinse the glassware with Milli-Q water, followed by a repeated rinse in boiling water. The latter is done to remove the ions absorbed in the cleaning solution from the glassware.
It should be noted that measurements in alkaline electrolytes should be made in a PTFE electrochemical cell due to glass corrosion.[58]

2.3.2. Preparation of the RDE/RRDE

Mechanical polishing of the electrode is performed before the electrochemical measurement. With this type of polishing, we remove scratches, gouges, and other damage on the electrode surface before the electrocatalyst is drop-casted.

We start with the largest particle size of alumina powder (1 μm). We apply 20 mg of alumina powder to the polishing layer and mix it with Milli-Q water. Next, we take the GC electrode and press it gently on the surface of the desired polish. For best results, polishing should be done with the pattern of the shape of the numeral 8 (or infinity symbol) with a constant force parallel to the surface of the polishing layer for 5 minutes. The RRDE electrode is then rinsed with Milli-Q water and placed in an ultrasonic bath for 15 sec. The process is then repeated with the 0.5 and 0.03 μm alumina powder particles.

2.3.3. Calibration of the reference electrode

Another important procedure prior to the electrochemical measurements is the calibration of the reference electrode. Since the ORR activity measurements are measured in potentiostatic mode (monitoring the electric current as a function of potential), the exact potential of the reference electrode in the electrolyte should be known.

Procedure: Calibration is performed by determining the zero current potential or open circuit potential (OCP) in a two-electrode system between the Pt working and reference electrodes in a saturated H_2 electrolyte. In OCP mode, the resting potential ($i = 0$) is measured between the working and reference electrodes. In the above example, the resting potential is determined when the reaction at the Pt working electrode ($2H^+ + 2e^- \leftrightarrow H_2$) is in equilibrium, and therefore, the net current flow is equal to 0. Note that for the correct potential of the reference electrode, the pH value of the electrolyte should be taken into account.

Procedure: To set up a two-electrode system, simply connect the counter electrode to the reference electrode and the signal to the working electrode cable. Then, connect the working electrode cable to the Pt wire and the reference counter electrode cable to the reference electrode in the electrochemical cell. Fill the electrochemical cell with electrolyte and purge the solution with H_2 gas for 5 minutes. Start the OCP measurement and determine the potential when it stabilizes.

2.3.4. Electrocatalyst preparation

The preparation of the homogeneous electrocatalyst layer on the surface of the RRDE electrode consists of two steps. The first is the preparation of a stable electrocatalyst dispersion in solution (electrocatalyst ink), and the second is the drop-casting of the electrocatalyst ink onto the RRDE electrode. To prepare a stable dispersion, we mix the prepared electrocatalyst with water, isopropanol, and Nafion. Nafion is a polymer used to provide ionic conductivity, flexibility, and better cohesion of the electrode and as a stabilizer to prevent aggregation in the suspension. The mixture is left in an ice bath under ultrasonic sonication for 40 minutes to obtain a homogeneous suspension before being dropped onto the surface of the electrode. While the droplet electrocatalyst is drying, the RRDE is rotated at 300 rpm. The rotation is to cause convection during drying and additionally to prevent aggregation of the nanoparticles and drying coffee ring effect.[59]

Procedure: Mix the electrocatalyst, deionized water, 2-propanol (IPA), and Nafion (5 wt.%. mixture of lower aliphatic alcohols and water) at the following ratio: 4.53 mg/0.83 mL/0.28 mL/30 μL. Place the mixture in an ice bath for 40 min until a homogeneous dispersion is formed using a horn sonicator (37.5 W). Next, drop-cast an aliquot of 25 μL onto a GC electrode and dry it on an inverse RRDE with a rotation of 300 rpm at room temperature 23 °C for 75 min (GC diameter = 5.5 mm, IPA/water = 24%).

2.3.5. Compensation of electrolyte resistance

In a three-electrode system (schematic representation of the electronic circuit in **Figure 14**), WE is the working electrode, CE is the counter electrode, RE is the reference electrode, R_f is the charge transfer resistance, C_{dl} is the double-layer capacitance, and R_u is the solution resistance. R_u is a function of cell geometry (distance between the working and reference electrodes), electrolyte conductivity, and (loading dependent) bubble formation within and on the catalyst layer[60] and can affect the potential between the working and reference electrodes.

Since cell geometry is difficult to determine, R_u must be measured. The three conventional methods for R_u measurement are electrochemical impedance spectroscopy, positive feedback, or current interrupt.[61,62]

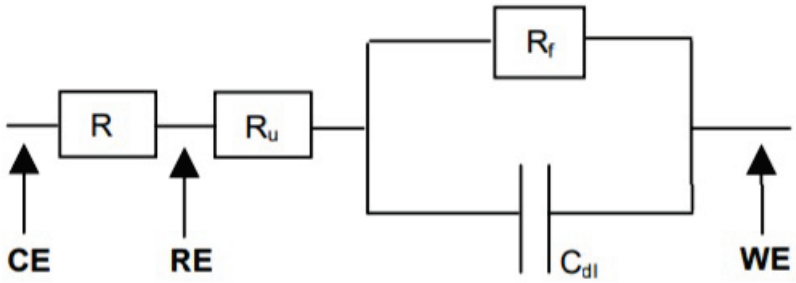

Figure 14: Schematic representation of a three-electrode system.[61]

For the measurement of the ohmic drop, we will use the positive feedback method. Here, the potential pulse is applied between the working electrode and a reference electrode while the current is monitored. During the measurement, the compensated resistance is increased until an oscillation of the measured current occurs. The oscillation is observed due to the full compensation of R_u, and the current becomes a function of capacitance. If overcompensation is achieved during the experiment, high oscillating currents will flow through WE, which may damage the electrocatalyst and electrode. Therefore, it is recommended that 80% of the total R_u value be compensated and 20% of the compensation be performed manually.[61]

Procedure: Fill the electrochemical cell with about 2 cm of electrolyte above the RRDE tip. Connect the counter electrode alligator cable to the carbon counter electrode, the reference electrode alligator cable to the 3M NaCl Ag/AgCl reference electrode, and the working electrode banana plug cable to the red connector on top of the Pine rotator. Then, purge the system with Ar gas for 5 minutes. Start the GPES software and press Utility/Positive Feedback at the top. Adjust the parameters as shown in **Figure 15**. Start the measurement and change the iR compensation bar (**slowly**) until oscillation occurs. Set the *iR* value to 90% of the total value relative to the start of the oscillation.

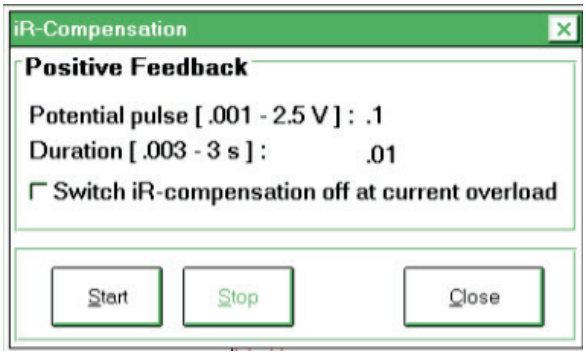

Figure 15: Parameters for the positive feedback IR compensation.

2.4. ORR characterization of Pt/C-based electrocatalysts

The base material used in PEMFCs for the ORR consists of platinum nanoparticles anchored on carbon supports (Pt/C).[63] Such Pt/C electrocatalysts are essential for the effective operation of PEMFC. However, to determine fully the performance of these electrocatalysts, in-depth analysis in the context of working fuel cells is essential. To perform this, the electrocatalyst must be integrated into catalyst-coated membranes or gas diffusion layers, which are then assembled into membrane electrode assembly (MEA). However, due to the high costs and complicated manufacturing process of MEA components, comprehensive in-situ evaluations are beyond the capabilities of many research institutes.[64]

As a practical alternative, research into the activity and stability of Pt/C electrocatalysts is often conducted using rotating disk electrode (RDE) studies in a simplified half-cell configuration with a liquid electrolyte. This simplified method serves as an effective method for preliminary screening. To prepare for testing, the Pt/C catalyst is first homogenized in an ink of alcohol, water, and a perfluorosulfonic acid ionomer, such as Nafion. This creates a stable dispersion, which is then applied in a precise aliquot to a GC disk electrode. The catalytic behavior is then investigated in a standard three-electrode electrochemical setup.[64]

The use of RDE as an investigative tool provides researchers with crucial insights into the kinetic aspects of ORR and the resilience of the electrocatalysts under simulated fuel cell operating conditions. Although RDE analysis is finer than a full-scale fuel cell test, it can closely mimic the dynamic electrochemical environment of a working PEMFC. This technique is central to the rapid modification and improvement of catalyst formulations and enables fast iteration cycles before materials are further developed for MEA integration and comprehensive fuel cell evaluations. Such a strategy is not only resource efficient but also drives the development of catalyst technology.[64]

Since the turn of the millennium, concerted efforts have been made to establish standard protocols and measurement parameters for RDE procedures on Pt/C.[65][66][67][68] The adoption of such standards is a fundamental step towards homogenizing research results and meaningful comparisons between different studies.

The standard values, as suggested by General Motors,[69] for a mass-specific activity (MA), area-specific activity (SA), and Pt electrochemical surface area (ECSA) of standard Pt/C electrocatalysts is essential are derived from a precise kinetic current measurement taken at 0.90 V vs. RHE during the ORR polarization curves. These measurements are performed at an electrode rotation rate of 1600 rpm, anodic scan direction, and a potential scan rate of 5 and 20 mV/s in an O_2-saturated 0.1 M $HClO_4$ electrolyte. These specific conditions were carefully selected to mimic real fuel cell environments while ensuring that the results were consistent and reliable.

Procedure:

i. **Preconditioning (*Ar saturated electrolyte solution*):** Select the method bar at the top of the GPES software and select Cyclic voltammetry (linear)*[1]. Select the following parameters: 50 cycles in the potential range 0.02 – 1.1 V vs RHE (**note that the potential range for the 3 M NaCl Ag/AgCl reference electrode should estimated using the equation $E_{RHE} = E_{Ag/AgCl} + E^{\circ}_{Ag/AgCl} + 0.059V \cdot pH$; the measured potential is corrected with the potential determine by OCP measurement 2.3.3.**) with a scan rate of 500 mV/s and a current range of 10 mA. Set the rotation rate of the RRDE to 1600 rpm and start the measurement.

The precondition is done to achieve a stable, reproducible signal and minimize the initial degradation of the catalyst due to nonhomogeneous drying. Preconditioning is performed with cyclic voltammetry in the same potential range as ORR activity is measured; however, it is done at a higher scan rate and several cycles.[70]

ii. **Baseline measurement:** The parameters and conditions are the same as for preconditioning; change the number of cycles from 50 to 5, the scan rate from 500 mV/s to 20 mV/s, and the current range from 10 mA to 1 mA.

iii. **ORR activity measurement:** Change the purge gas from Ar to O_2, wait 15 minutes until the electrolyte is saturated with O_2 gas, and start the measurement (same parameters as *for ii Baseline measurement*).

*[1] The difference between the staircase mode and the linear mode is the time taken to record the current after the potential change. This enables studying two types of electrochemical processes: fast (non-double layer charging) and slower processes (Faradaic reactions).

A) Determination of MA, SA and $ECSA_{Pt}$

The MA is calculated by determining the kinetic current (i_k) using **Equation (11)** and then normalizing this current to the total mass of Pt on the disk electrode (**Equation 12**).[64]

$$i_k = \frac{i_{lim} \times i_m}{i_{lim} - i_m} \tag{11}$$

$$MA = \frac{i_k}{m_{Pt}} \tag{12}$$

Here, i_{lim} denotes the limiting current measured at E = 0.50 V vs. RHE, and i_m stands for the measured current at E = 0.90 V vs. RHE.[64]

Similarly, the area SA is calculated (**Equation 14**) by taking i_k and normalizing it with respect to the platinum $ECSA_{Pt}$, using **Equation (13)**.[64]

$$ECSA_{Pt} = \left(\frac{Q(C)}{210 \mu C\, cm_{Pt}^{-2} \times L_{Pt} \times A_g}\right) \times 10^5 \tag{13}$$

$$SA = \frac{i_k}{ECSA_{Pt}} \tag{14}$$

Here, L_{Pt} ($\mu g_{Pt} cm^{-2}$) is Pt loading on the electrode, and A_g is the geometric surface area of the glassy carbon electrode. The Q(C) represents charge from hydrogen underpotential (H_{UPD}) and is derived from the integration under the CV curve between 0.40 V and 0.05 V during the negative scan direction and correcting for the double layer charge current measured at 0.40 V vs. RHE, as shown in **Figure 16**, using **Equation 15**.[64]

$$Q(C) = \frac{1}{v} \int_{\frac{E_1 - E_0}{v}}^{\frac{E_2 - E_0}{v}} i dE \tag{15}$$

Where E is potential, i electric current, and v scan speed (V/s).

In CV studies, two different peaks are typically characterized by the H_{UPD}: an adsorption peak and a desorption peak. These peaks occur before the region where hydrogen gas evolution takes

place, which is why they are also referred to as “underpotential”. The amount of electricity (charge) involved in the adsorption of a monolayer of hydrogen atoms is known for a given metal in a specific electrolyte and allows the calculation of the actual metal surface accessible for catalytic reactions. For a monolayer of hydrogen atoms adsorbed on a platinum surface in an acidic environment, this charge is 210 $\mu C cm_{Pt}^{-2}$.[6471]

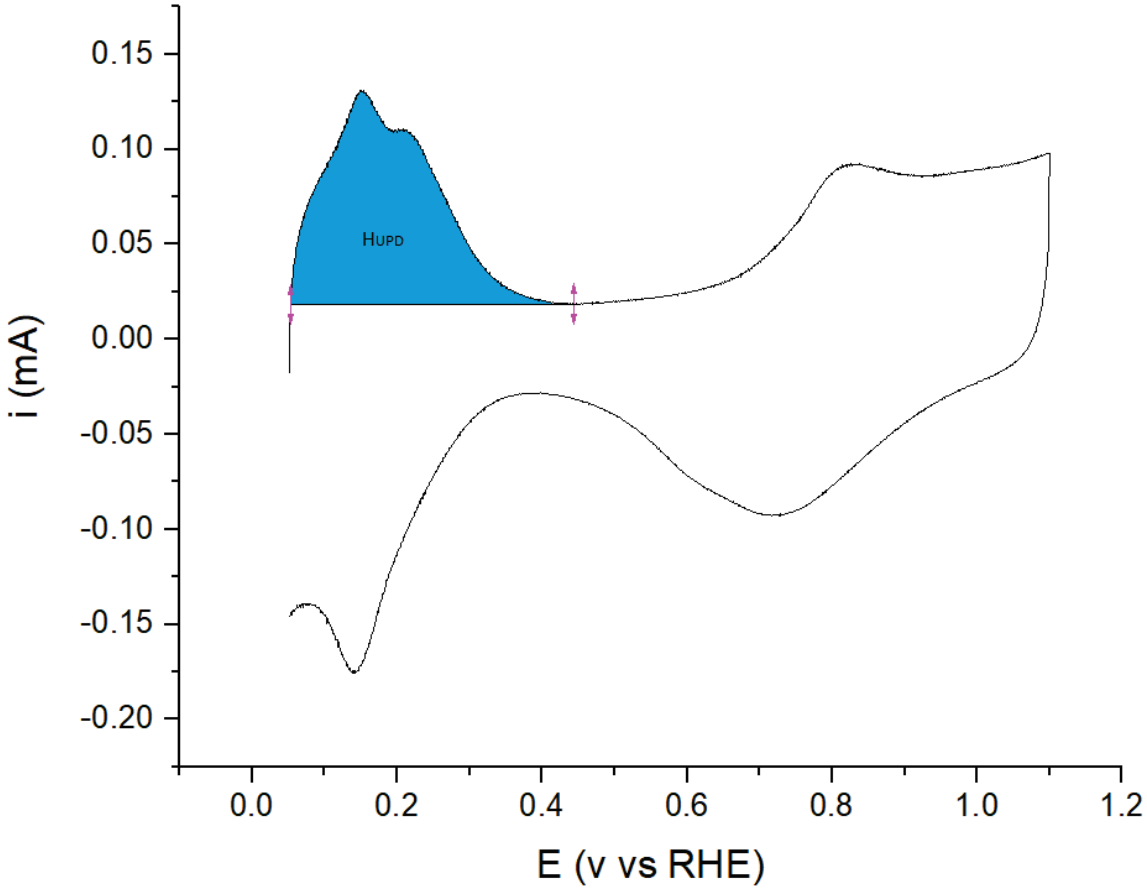

Figure 16: CV polarization curve of Pt/C electrocatalysts in Ar saturated 0.1 M $HClO_4$ at 20 mV/s scan rate and 1600 rpm rotation rate. The H_{UPD} area is presented marked blue.

The specification of the ECSA normalized to the platinum mass allows a direct comparison of the performance of different catalysts independent of their platinum charge. This normalization is particularly important in catalysis research, for which the cost of platinum is an important factor in the overall feasibility of fuel cell technology. By providing a measure of ECSA relative to the amount of platinum used, researchers and engineers can optimize the design and use of platinum in catalytic systems, potentially leading to more cost-effective and sustainable fuel cell technologies.[64]

Questions

1. With the help of equations 11–15, calculate the ESCA, MA, and SA of measured Pt/C electrocatalysts.

2. What is the reason for using the anodic sweep direction when measuring the kinetic current (i_k) during CV?

3. In addition to hydrogen underpotential desorption, what alternative techniques are available to determine the electrochemical surface area (ECSA) of Pt-based electrocatalysts?

4. What are the current state-of-the-art electrocatalysts used for ORR in PEMFC? What methods to further improve efficiency are being utilized?

5. How do variations in scan rate and rotation speed of the RDE/RRDE affect the observed current density in Ar and in O_2 saturated 0.1 M $KClO_4$ solutions? What are the reasons for these effects?

2.5. Measuring HER and OER activity on nickel-based catalyst material

Electrochemical production of hydrogen and oxygen by water dissociation using suitable catalysts (electrocatalytic water splitting) is a common source and a reliable technology for hydrogen/oxygen production compared to other conventional methods. The electrochemical process of water splitting into hydrogen and oxygen is called Hydrogen Evolution Reaction (HER: reduction/cathodic process) and Oxygen Evolution Reaction (OER: oxidation/anodic process), respectively. Platinum and other PGM catalysts are found to be the best catalysts for these reactions; however, they are expensive and scarce, which has led to finding cheaper but efficient replacements. Nickel has been a fitting candidate and is relatively cheap and abundant. In this experiment, we will analyze the HER and OER activity of a commercial Nickel on carbon catalyst material (Ni/C) using an RDE setup (**Figure 17**). Here, nickel is present in the metallic phase (Ni^0) and is homogenously mixed with conductive carbon black (Vulcan carbon). Cyclic voltammetry (CV) and Electrochemical Impedance Spectroscopy (EIS) will be used for electrochemical characterization.[72,73]

Materials and setup:

A 3-electrode set-up is used: RDE with Ni/C catalyst film as working electrode (WE), Graphite rod as counter electrode (CE), and Ag/AgCl/3M NaCl electrode as reference electrode (RE). 0.1 M KOH is used as an electrolyte. The RDE (rotating disk electrode) has a glassy carbon disk embedded in Teflon collette.

Procedure:

Electrode preparation (ink drop-casting):

Mix the Ni/C electrocatalyst, Milli-Q water, 2-propanol (IPA), and Nafion (5 wt.%. mixture of lower aliphatic alcohols and water) in the following ratio: 1.5 mg/0.8 mL/0.2 mL/10 µL. Place the mixture in an ice bath for 20 min until a homogeneous dispersion is formed using an ultrasound sonicator. Then, drop-cast an aliquot of 20 µL onto a clean, polished glassy carbon electrode (GC) and dry it on an inverse RDE with a rotation of 500 rpm at room temperature for 1 hour (GC diameter = 5 mm). A thin, uniform catalyst layer/film should be obtained.

Assembly of the electrochemical cell:

Assemble the three-electrode system in the electrochemical cell and fill the cell with freshly prepared electrolyte. Purge the electrolyte with argon (or nitrogen) for at least 15 minutes before the measurements to remove dissolved oxygen. Once the cell is ready, connect the potentiostat to the cell and ensure there is proper connection (contact) and no bubbles in the salt-bridge. Once this is done, slowly immerse the RDE (with catalyst film) in the electrolyte to enable rotation (3600 rpm).

Electrochemical Measurements: Protocol

Immersion of RDE into the electrolyte is to be done at -0.965 V Ag/AgCl (0 V RHE) to prevent oxidation/reduction that might occur at OCP or other potentials that can alter the active catalyst species.

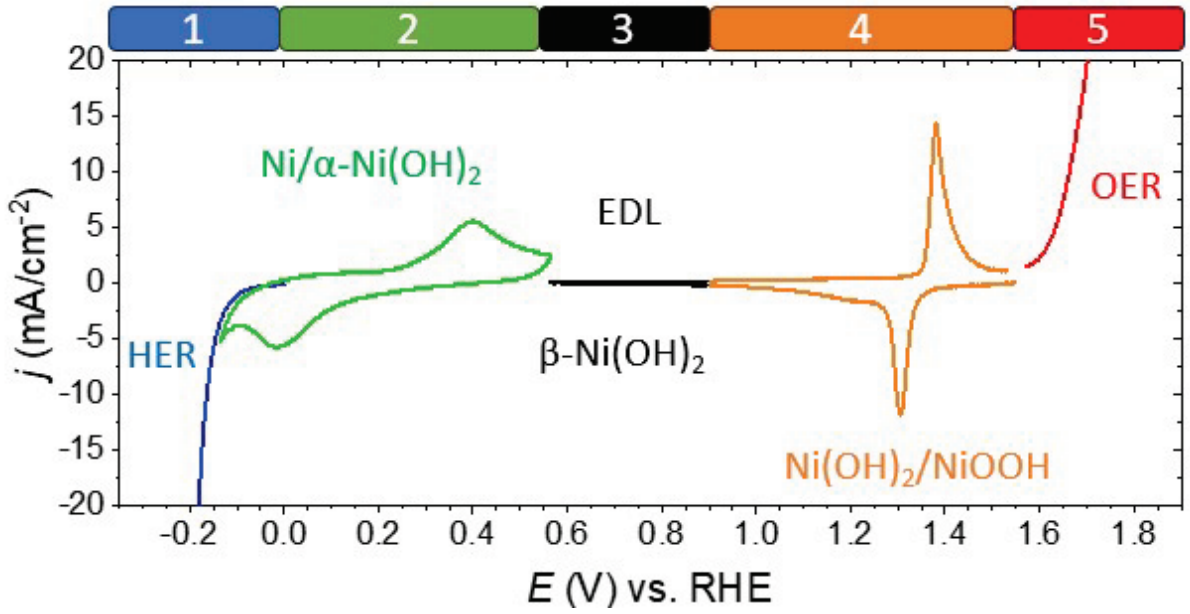

Figure 17: Main voltammogram features shown by Ni catalysts in an alkaline aqueous medium within a wide potential range, divided into 5 regions: (1) HER region, (2) Alpha-peak: Redox couple of Ni^0 / α-$Ni(OH)_2$, (3) Electric Double layer region, no faradaic reaction, but involves phase transformation of α- to β-$Ni(OH)_2$, (4) Oxyhydroxide peak: Redox couple of $Ni(OH)_2$/Ni(OOH), (5) OER region.[74]

HER:

Perform cyclic voltammetry (CV) with a scan rate of 0.05 V/s. The potential range should be -1.5 V to 0.4 V vs. Ag/AgCl. This includes the HER region and a Ni^0/Ni^{2+} redox transition peak. Five scans are to be done. The lower potential limit can be adjusted to obtain a good HER polarization curve (current range to be noted).

OER:

Perform CV with a scan rate of 0.05 V/s within the potential range of 0.4 V to 0.785 V vs. Ag/AgCl. This includes a Ni^{2+}/Ni^{3+} redox transition peak and the OER region. Five scans are to be done. Avoid high potentials so as not to damage the GC disk.

iR correction:

The *iR* drop (or potential drop) is essentially the decrease in applied potential on the working electrode surface (electrochemical double layer); here, the *R* (resistance) is also referred to as the non-compensated electrolyte resistance (R_s = resistance of solution between working electrode surface and reference electrode). Electrolyte resistance can be measured by EIS at a potential where no faradaic reaction occurs, and in this case, preferably at -0.965 V vs. Ag/AgCl. Since *R* in *iR* compensation can also include contributions from connection/contact resistance, catalyst resistance, cell geometry (distance between the working and reference electrodes), electrolyte conductivity, and (loading dependent) bubble formation within and on the catalyst layer,[60], slopes from Tafel plot (*E* vs log *I*) are to be cross-checked after compensation of R_S to determine if it is under/over-compensated and adjusted accordingly (partial compensation was avoided). This is important as it can lead to major discrepancies in the values of current/activity when current is significantly high (**Figure 18**).[75]

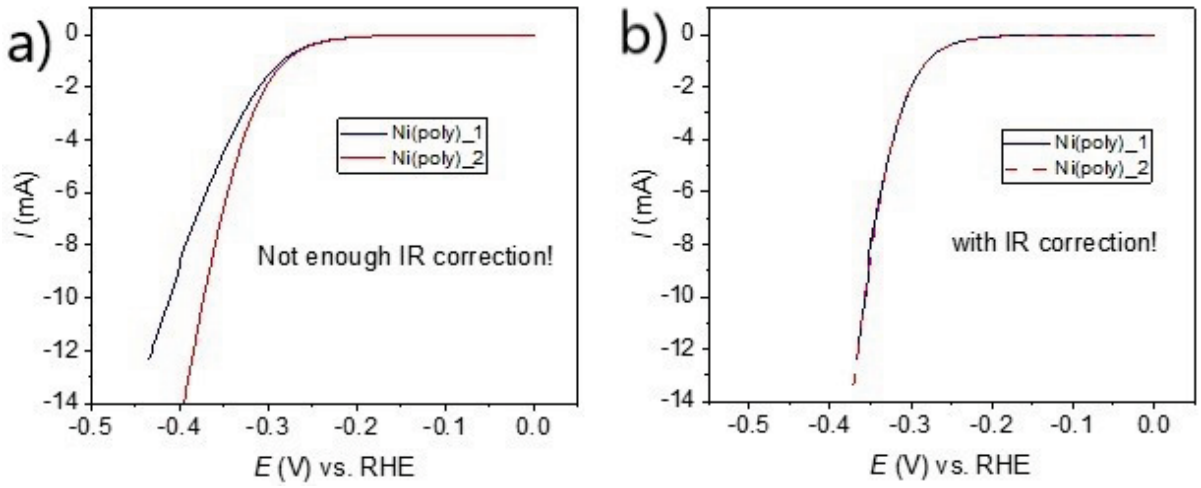

Figure 18: An example demonstrating the relevance of proper iR compensation. A HER polarization curve performed with the same Ni-based sample on two different days a) without and b) with complete compensation.[74]

Data Collection and Treatment:

Export the data from Nova software as a text file and import it into Origin software. The data will be imported as columns of potentials and corresponding current values obtained. Perform the *iR* correction for electrolyte resistance (this value is obtained from EIS) by multiplying the absolute current with the electrolyte resistance. Use this corrected value for further plotting and calculations. Also, calculate the geometric current density, *j*, by dividing the current by the glassy carbon disk area. Report it in mA/cm². Plot the CV (potential vs. *j*) and corresponding Tafel plot (potential vs. log of the current density *j*) in Origin. Tafel slope will also provide an idea of whether there is any under-compensated (or overcompensated) resistance; in such case, add (or subtract) a few more ohms in the *iR* correction equation. Proper *iR* compensation is essential to understanding and explaining activity from a CV.

Exercises

1. Calculate HER and OER activity using geometric current density: From the CV (with compensated potential vs. current density), calculate the overpotential for both HER and OER, which is the potential at which a noticeable current density (e.g., 5 mA/cm²) is observed for 1st and 5th scan.

2. Calculate specific activity for HER: Take the 5th scan of the HER protocol and integrate the oxidation peak of Ni^0/Ni^{2+} redox couple. Record this peak area from the integration in Ampere. Volt (A.V) and divide this by scan rate (V/s) to obtain the charge (A.s = coulomb C). Divide the raw current (in mA) with this charge and multiply it with 516 µC/cm², which corresponds to the charge for monolayer hydroxide formation. The obtained value corresponds to the current density (j_{spec}=mA/ cm²) that represents specific activity. Be careful during unit conversion.

3. Calculate mass activity; the mass of Ni was calculated for the given powder sample based on the amount of nickel species present in the deposited ink (Ni loading). [e.g., the catalyst ink contains 1 mg of catalyst powder dispersed in 1 mL solution. ~20 µL of the ink is deposited and measured, which corresponds to ~20 µg of catalyst material on the disk. For 20% Ni on C material, the amount of Ni present on the disk is 20% of 20 µg = 4 µg of Ni. Similarly, the mass of Ni is to be calculated for the given Ni/C sample based on the ink composition used]. The values of current (raw data) are divided by the mass of Ni to find the mass activity of the catalyst (unit- mA/μg_{Ni}). Report the mass activity by taking the current @ -1.3 V Ag/AgCl for the 5th scan.

2.6. ORR performance of non-metal electrocatalysts

Platinum-carbon-based catalysts have been the focus of research, with most studies focusing on reducing cost and increasing electrocatalytic performance.[20] Among the most promising methods, the use of Pt nanoparticles, Pt alloys combining Pt with transition metals such as cobalt (Co), nickel (Ni), or iron (Fe) also further increased ORR activity.[21] Another method that consumes less Pt and maximizes Pt surface area is the preparation of core-shell catalysts. These catalysts are composed of core material (often a cheaper metal) deposited to carbon support covered by a thin Pt shell. Materials to boost the stability of support have also been developed. Among them, modified carbon-based catalyst supports with high graphite content have shown to be advantageous, such structures based on graphene derivatives.

To further decrease the cost of ORR electrocatalyst, Pt was replaced by transition metals. The most promising material in this group is the metal-nitrogen-carbon catalyst (M-N-C), in which transition metals are coordinated with nitrogen in a carbon matrix. Examples are iron-nitrogen-carbon (Fe-N-C) or cobalt-nitrogen-carbon (Co-N-C) catalysts.[4]

Additionally, to reduce the cost of ORR electrocatalysts, the development of completely metal-free catalysts based on carbon has been established. Materials such as graphene or carbon nanotubes have been explored as potential ORR catalysts. Often, these materials are doped or combined with other elements (boron, nitrogen, oxygen, fluorine, sulfur, etc.) to enhance their catalytic activity. Among them, N-doped graphene derivatives are proving to be particularly promising. Their unique electronic structure, resulting from the synergy between the inherent conductivity of graphene and the electron-rich properties induced by nitrogen doping, offers enhanced ORR activity. In addition, their large surface area, tunable porosity, and structural robustness make them exceptionally resilient under fuel cell operating conditions.[1,18,19,27]

Procedure:

i. **Preconditioning (*Ar saturated electrolyte solution*):** Select the method bar at the top of the GPES software and select Cyclic voltammetry (linear)*.[2] Select the following parameters: 50 cycles in the potential range 0.02 – 1.1 V vs. RHE (**note that the potential range for the 3 M NaCl Ag/AgCl reference electrode should estimated using the equation $E_{RHE} = E_{Ag/AgCl} + E^{\circ}_{Ag/AgCl} + 0.059V \cdot pH$; the measured potential is corrected with the potential determine by OCP measurement 2.3.3.**) with a scan rate of 500 mV/s and a current range of 10 mA. Set the rotation rate of the RRDE to 1600 rpm and start the measurement.

*[1] The difference between the staircase mode and the linear mode is the time taken to record the current after the potential change. This allows us to study two types of electrochemical processes: fast (non-double layer charging) and slower processes (Faradaic reactions).

ii. **Baseline measurement:** The parameters and conditions are the same as for preconditioning; change the number of cycles from 50 to 5, the scan rate from 500 mV/s to 20 mV/s, and the current range from 10 mA to 1 mA.

iii. **ORR activity measurement:** Change the purge gas from Ar to O_2, wait 15 minutes until the electrolyte is saturated with O_2 gas, and start the measurement (using the same parameters as for *ii Baseline measurement*).

iv. **ORR selectivity measurement with RDE:** Repeat the measurements with a rotation rate of 400, 625, 900, and 1225 rpm (the same parameters as for *ii. Baseline measurement*).

v. **ORR selectivity measurement with RRDE:** Change the rotation rate to 1600 rpm additionally connect the WE2 cable to the blue banana plug on the top of the rotator (same parameters as for *ii Baseline measurement*, with additional potential of WE2 at 1.3 V vs. RHE) and start the measurement.

vi. **Determination of collection efficiency:** Change the purge gas back to Ar. Add 10 mL of 10 mM $[Fe(CN)_6]^{-3}$ to the electrolyte solution (adjust the initial and final potential if you know that $[Fe(CN)_6]^{-3} + e^- \leftrightarrow [Fe(CN)_6]^{-4}$, $E° = 0.361$ V vs. RHE and the potential of WE2 at $E = E_{[Fe(CN)6]-3\ /[Fe(CN)6]-4}$ V vs. RHE + 0.2 V); the other parameters are the same as for (**ii. Baseline measurement**); and start the measurement.

vii. **ORR stability measurement (*O_2 saturated electrolyte solution*):** Change the purge gas from Ar to O_2, and wait until the electrolyte is saturated with O_2 (ca 15 minutes). Select Methods/Chrono methods (interval time >.1s)/Amperometry. Set the potential to 0.7 V vs. RHE for acidic electrolytes (pH = 1) or 0.3 V vs. RHE for alkaline electrolytes (pH = 13), the duration to 7200 s, and start the measurement. The potentials in alkaline and acid electrolytes for stability measurements are chosen at different values due to the different activity and the associated different kinetic-diffusion current ranges.

A) Determination of ORR activity from onset potential (E_{onset})

For non-metal electrocatalysts, the main method for determining ORR activity is the E_{onset}. Unfortunately, in the literature, the E_{onset} is poorly defined but is usually represented by the point at which the baseline and the steepest tangent to the slope of the ORR polarization curve intersect (as seen in **Figure 19**).[76] The second method is to determine the potential at which the current density reaches 0.1 mA/cm².[77]

a. Subtract the current for the **baseline** from the **ORR** cyclovoltammetry measurement.
b. Convert the potential from V vs. Ag/AgCl to V vs. RHE by subtracting the OCP in H_2 saturated solution.

c. Convert the disk current to disk current density by dividing the current by the electrode surface area (d = 5.5 mm)
d. Select the anodic current (direction from 0.02 to 1.1 V vs. RHE) and determine the E_{onset} with the tangent method as is shown in **Figure 19** and by the potential at 0.1 mA/cm² current density.

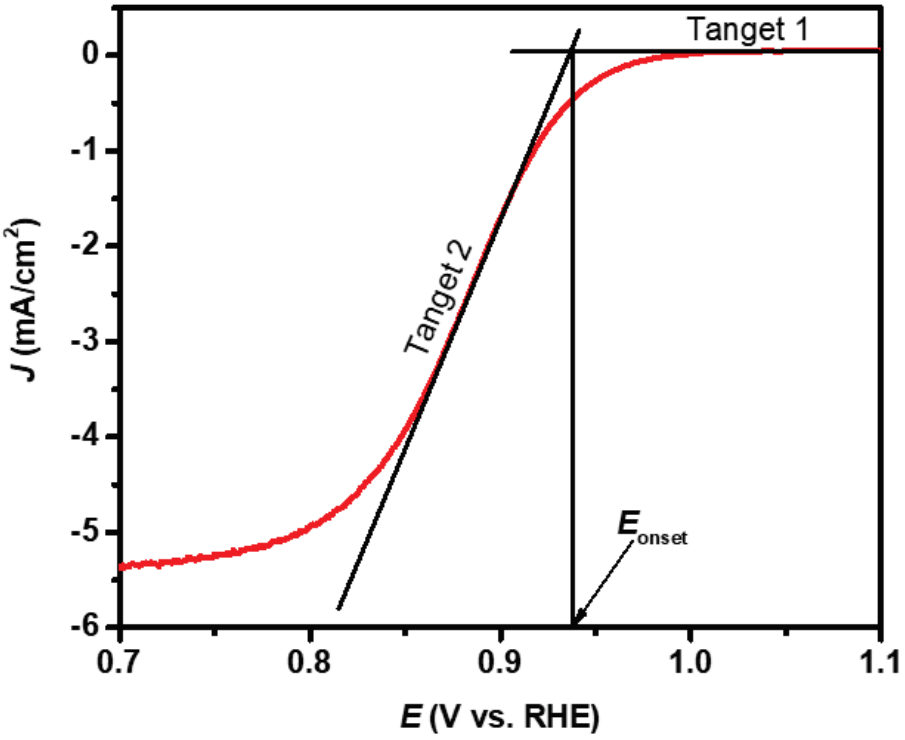

Figure 19: Schematic representation of tangential onset potential determination.

B) Determination of ORR selectivity by RDE

a. Subtract the current for the **baseline** from the **ORR** cyclovoltammetry measurement at rotation speeds 400, 625, 900, 1225, and 1600 rpm.
b. Convert the potential from V vs. Ag/AgCl to V vs. RHE by subtraction of measured potential from the OCP.
c. Plot $i^{-1}_{DC,0}$ vs. $\omega^{-1/2}$ at E = 0.1, 0.2, 0.3 ... 0.8 V vs. RHE and calculate the number of transferred electrons using **Equation (10)**.

For the constants **in O_2 saturated 0.1 M $HClO_4$** use F = 96500 As/mol, electrode diameter = 5.5 mm, D_{O2} (diffusion coefficient) $2.0 \cdot 10^{-5}$ cm²/s, ν = 0.01 cm²/s) and C_O = $1.2 \cdot 10^{-6}$mol/cm³).[78]

For the constants **in O_2 saturated 0.1 M KOH** use F = (96500 As/mol), electrode diameter = 5.5 mm, D_{O2} the diffusion coefficient ($2.2 \cdot 10^{-5}$ cm²/s), ν (0.01 cm²/s) and C_O ($1.13 \cdot 10^{-6}$ mol/cm³).[79]

C) Determination of ORR selectivity with RRDE

a. Calculate the collection efficiency (N), according to **Equation (16)** (current should be chosen in the diffusion-convection limited region):

$$N = \left| \frac{i_{r,[Fe(CN)6]-4}}{-i_{d,[Fe(CN)6]-3}} \right| \quad (16)$$

Where $i_{d,[Fe(CN)6]-3}$ is the disk current from the reduction of $[Fe(CN)_6]^{-3}$, and $i_{r,[Fe(CN)6]-4}$ is the ring current from the oxidation of $[Fe(CN)_6]^{-4}$.

b. Subtract the **baseline** from the **ORR** cyclovoltammetry measurement with RRDE.
c. Convert the potential from V vs. Ag/AgCl to V vs. RHE by subtracting the OCP in H_2 saturated solution.
d. Calculate the number of transferred electrons according to **Equation (17)** at E = 0.1, 0.2, 0.3 ... 0.8 V vs. RHE.

$$n = \left| \frac{4NI_d}{NI_d + I_r} \right| \quad (17)$$

D. Determination of the ORR stability

Determine the electric current ratio between the current after 7200 seconds and at the beginning of the chronoamperometric measurement ($\frac{i_{t=7200}}{i_{t=0}}$). Write the result in %.

$$\frac{i_{t=7200}}{i_{t=0}}\ (\%) =$$

Questions

1. What is the difference between Faradaic and non-Faradaic processes?

2. What is the driving force for ion migration, diffusion, and convection in mass transport?

3. During ORR measurement at the working electrode, how much current flows through the reference electrode and how much through the counter electrode? For which processes is the current at the counter electrode used when the ORR takes place at the working electrode?

4. Define NHE, SHE, and RHE.

5. What are the differences between RDE and RRDE selectivity measurements? Which method is better for selectivity measurements?

6. From **2.3.4 Electrocatalyst preparation**, calculate the electrocatalyst loading (*L*)–- the mass of the electrocatalyst normalized to the working electrode surface area (μg/cm²).

3. The structural, chemical, and physical characterization of graphene derivatives

Due to the unique bulk and surface structure, trace impurities, and graphitic structure, the methods for characterizing graphene derivatives are diverse. Characterization methods such as atomic force microscopy (AFM), scanning electron microscopy (SEM), transmission electron microscopy (TEM), and high-resolution transmission electron microscopy (HRTEM) provide more detailed insight into the morphology and structure of graphene derivatives. For chemical composition, spectroscopic methods such as X-ray photoelectron spectroscopy (XPS), Fourier transform infrared spectroscopy (FTIR), ultraviolet-visible spectroscopy (UV VIS), or thermal analysis coupled with mass spectroscopy (TA-MS) are usually used. X-ray diffraction (XRD) and Raman spectroscopy are used to provide additional information on the graphitic structure of graphene derivatives. Trace metals are analyzed by inductively coupled plasma mass spectrometry (ICP-MS), inductively coupled plasma optical emission spectroscopy (ICP-OES), nuclear activation analysis (NAA), or X-ray fluorescence. Finally, surface area information is derived using the Brunauer-Emmett-Teller (BET) theory of surface analysis.[80,81]

Although there is a wide variety of methods for characterizing graphene derivatives, we will focus on the most routinely used ones. In the following chapter, we will characterize the prepared graphene derivatives using Raman, XPS, TA, BET surface analysis, ICP-MS, and SEM methods.

3.1. Raman spectroscopy

In 1928, physicist C. V. Raman observed that the wavelength of light scattered by molecules depends on the wavelength of the incident light source and later that the change in wavelength of the scattered light depends on the chemical structure of the molecules. For his discoveries and further research in the field of Raman spectroscopy, he was awarded the Nobel Prize in Physics in 1931.[82]

In Raman spectroscopy, the sample is irradiated with an intense monochromatic photon source (laser) whose wavelength is visible or near the IR light range. Due to the low intensity of Raman scattering (0.001% of the light source), Raman spectroscopy was rarely used until the development of the laser. For a molecule to be Raman active, it must exhibit the interaction between the electron field of the monochromatic light source and the electron cloud of the molecule, inducing the dipole in the molecule. Thus, the higher the polarizability of the molecule, the higher the intensity of the Raman peaks. The Raman spectrum is obtained by subtracting the inelastically scattered photons from the wavelength of the incident photons.[82,83]

The mechanism of Raman scattering is shown in **Figure 20**. When the sample is irradiated with a light source of energy $h\nu_0$ (wavelength in the visible or near IR spectral range), three processes can occur. First is elastic scattering or Rayleigh scattering, in which the energy of the scattered light remains equal to the energy of the incident light. Second, the phonon (quantum-mechanical description of vibrations of the atoms or molecule in the lattice) ground energy state (E_0) of the molecule is excited to a virtual phonon energy level with a photon (energy $h\nu_0$). Subsequently, the relaxation of the virtual energy level to the energy level ($E_0 + h\nu_{vib}$) occurs, and the photon with energy $h(\nu_0 - \nu_{vib})$ is emitted. The emitted photon scattered with lower energy than the incident one is called “Stokes scattering”. The third process is opposite to Stokes scattering and is called “anti-Stokes scattering”. The energy level $E_0 + h\nu_{vib}$ is brought to a virtual energy state with energy $h\nu_0$ and then relaxed in the E_0 phonon level, emitting the photon with higher energy $h(\nu_0 + \nu_{vib})$.[82,83]

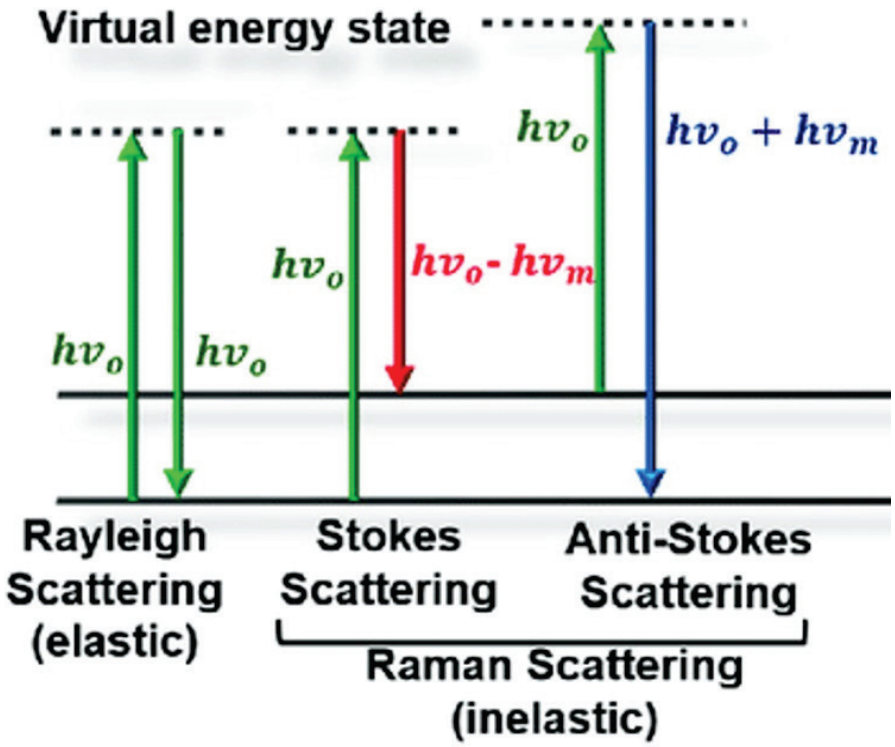

Figure 20: Energy level diagram for Rayleigh and Raman scattering.[84]

Raman spectroscopy is one of the most widely used, high-throughput, and non-destructive techniques to obtain information about the graphitic structure of graphene derivatives. However, to better understand the Raman spectra of graphene, we must first delve into the rather complex vibration theory of graphene.[80]

Single-layer graphene consists of carbon atoms, each bonded to three adjected carbon atoms in the form of a honeycomb. The Bravais lattice (a space that, when translated by a subset of all vectors fills the lattice space without overlap or voids) of the graphene crystal lattice consists of two carbon atoms, as shown in **Figure 21 a**).[85]

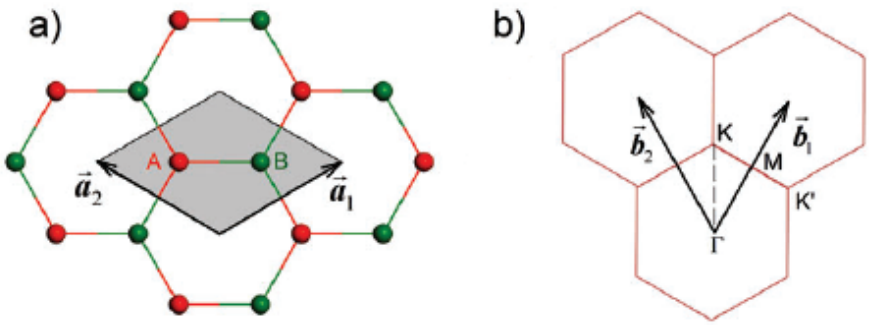

Figure 21: a) The top view of the Bravais lattice of single-layer graphene and b) The unit cell of the reciprocal space of single-layer graphene, with its high symmetry points and axes.[85]

To study a periodic system such as the lattice of crystal structures, the mathematical description of the structural symmetry must be approached. For this reason, the Fourier transformation of the Bravais to the reciprocal lattice (as seen in **Figure 21 b**) is performed, and the conclusions about the material properties follow logically in terms of the symmetry points (Γ, M, K, and K'). The reciprocal lattice provides a way to visualize the result of the Fourier transformation of the spatial (in our case, 2D) function. Similarly, the Fourier transformation is performed for the transformation from the time domain to the frequency domain to produce the classical IR spectra during FTIR spectroscopy.[85]

Next, we must deal with the phonon modes (quantum-mechanical description of the vibrations of the atoms or molecules in the lattice). As mentioned earlier, there are two carbon atoms in the single-layer graphene unit cell that are responsible for six different phonon modes at Γ, which corresponds to an irreducible representation of symmetry, as shown in **Figure 22**. Three phonon modes are acoustic (motion of two carbon atoms in the same direction, an A_{2u} and doubly degenerate E_{1u}) and three are optical (motion of two carbon atoms in the opposite direction, a doubly degenerate E_{2g}, and B_{2g}).[85]

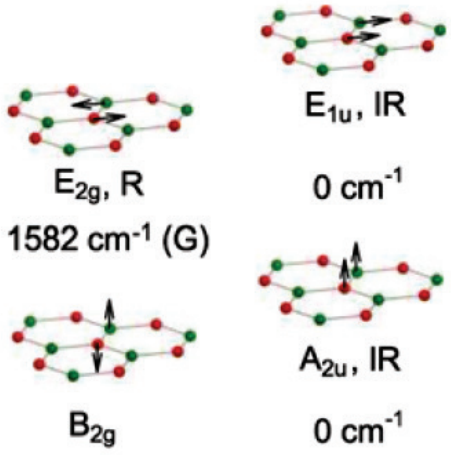

Figure 22: Displacements of phonon modes at the Γ points of single-layer graphene. The red and green dots represent nonequivalent carbon atoms. Black arrows show the atomic displacements for each mode. The Raman-active) and infrared-active (IR) modes are labeled.[85]

Density functional perturbation theory can be used to determine the information about the atomic vibrations at the Γ point of the phonon dispersion of single-layer graphene. The active Raman mode (the G-band) of single-layer graphene is at 1580–1605 cm^{-1}. The G band is a characteristic peak of graphene-related materials and is related to the doubly degenerate longitudinal optical (LO) and in-plane transverse optical (TO) E_{2g} phonon modes at the Γ point. The corresponding characteristic modes of the 2D and the D require additional defects in the graphene structure to be Raman active and are, therefore, not present in the Raman spectrum of pristine single-layer graphene. Since defects such as edges are naturally present in the graphene structure, the D and 2D peaks are normally observed for single-layer graphene in Raman spectra.[85]

In the Raman spectra, the three main peaks used to characterize the defect density and the number of graphene layers are D (1320–1350 cm^{-1}), G (1580–1605 cm^{-1}), and 2D (2640–2680 cm^{-1}), as shown in **Figure 23**.[80,86]

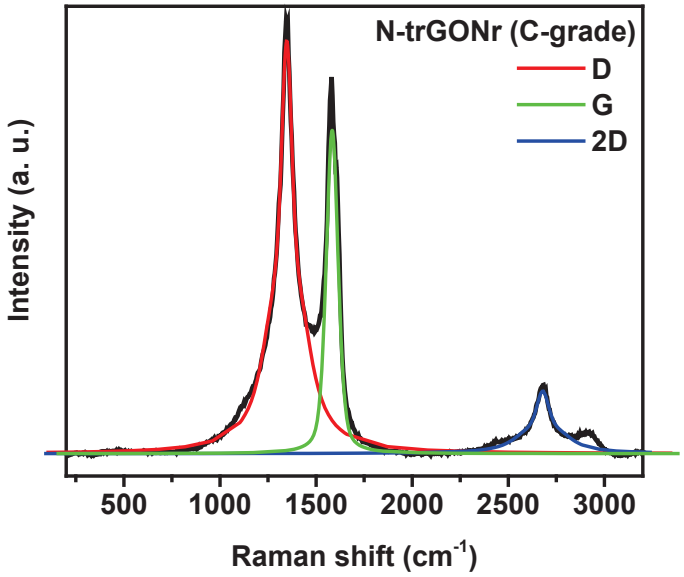

Figure 23: Example of Raman spectra of N-doped graphene derivative.

The appearance of the D peak in the Raman spectra is due to impurities and structural defects. If we know the intensity ratio between the D peak and the G peak, we can determine the average distance between the defects in the graphene structure. Using the Raman spectra, we can also speculate on the number of graphene layers by comparing the intensity ratio of the 2D and G peaks. A 2D/G intensity ratio of two is representative of single-layer graphene, a ratio of one is representative of bilayer graphene sheets, and a lower ratio is representative of few and multilayer graphene sheets.[80,86]

Exercise 1

1. From the intensities of the D, G, and 2D peaks in the Raman spectra, determine the number of graphene layers and the average distance between defects (L_D) for CVD-grown graphene and thermally exfoliated (TE) graphene derivatives.

Layer # (CVD) = Layer # (TE) =

Questions

1. Explain the nature of light interaction with the molecule in Raman spectroscopy. What is polarizability?

2. From the point of view of quantum mechanics, which type of inelastic light scattering is more probable and, therefore, has higher intensity?

3. The intensity of Raman spectra follows the equation $I \approx \nu^4$, i.e., the intensity of blue (400 nm) is 16 times higher than that of red (800 nm). If we use UV light, the intensity is even higher. Why is the light used for Raman spectroscopy limited by the light frequency, and why is the use of blue (400 nm) light rare?

4. Given the distance between the A and B carbon atoms ($d_{A\text{-}B}$ = 0.142 nm), calculate the lattice constants $\overrightarrow{a_1}$ and $\overrightarrow{a_2}$ in **Figure 21 a)**.

5. Which type of synthesis (bottom-up or top-down) yields a more "precise" graphene structure by comparing the number of graphene layers and the L_D from **Exercise 1**?

3.2. X-ray photoelectron spectroscopy (XPS)

XPS is a non-destructive, surface-sensitive, and quantitative spectroscopic technique. XPS spectra are obtained by irradiating the sample in a vacuum with monochromatic X-rays (usually Mg K_α at 1253.6 eV or Al K_α at 1486.6 eV) and detecting the kinetic energy of the ejected core electrons (1–10 μm deep). The emitted electrons have a kinetic energy equal to:[80]

$$KE = h\nu - BE - \phi_s \tag{18}$$

where *KE* is the kinetic energy of the electron, *BE* is the binding energy of the atomic orbital from which the electron originates, $h\nu$ is the energy of the X-rays, and ϕ_S is the work function (additional potential energy required by the electrons to leave the surface of the sample due to the energy difference between the sample and the spectroscope) of the spectroscope and is determined by calibration.[87]

Because of the characteristic *BE*, XPS can be used to identify and quantify the elemental surface concentration and chemical state (from the small variations of *BE* resulting from the polarizability and chemical potential of the compound) of the materials.[87]

When a core electron is emitted, there are generally two processes that can occur when an empty low-energy nuclear orbital is filled with electrons from higher-energy orbitals. One is X-ray fluorescence (a minor process), and the other is the emission of Auger electrons. The electrons are then directed to the detector by a mass analyzer operating in a specific energy window (pass energy).[87]

We will use XPS to characterize the surface chemical structure of graphene derivatives. We will also study the types of nitrogen configuration with the deconvolution of the N *1s* peak. In the XPS spectra, we can identify four main nitrogen configurations (as shown in **Figures 24** and **27**): pyridinic-N (397.7 – 397.4 eV), pyrrolic-N (398.7 – 399.0 eV), graphitic-N (400.2 – 400.6 eV), and oxidized-N at binding energies (402.4 – 402.8 eV). Among the N configurations, pyrrolic-N is assumed to be the most active for ORR.[88,89,90]

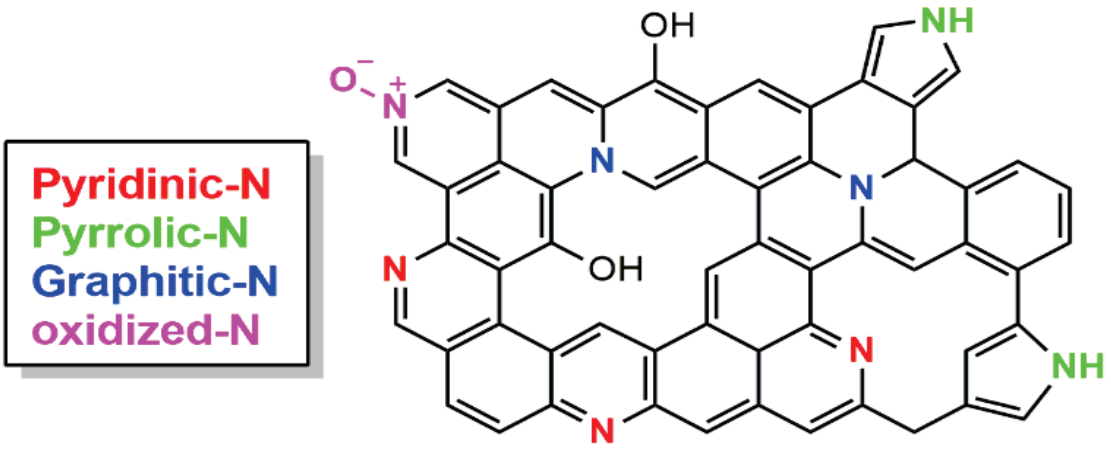

Figure 24: Molecular schematic of the different nitrogen configuration types of N-doped graphene derivatives.

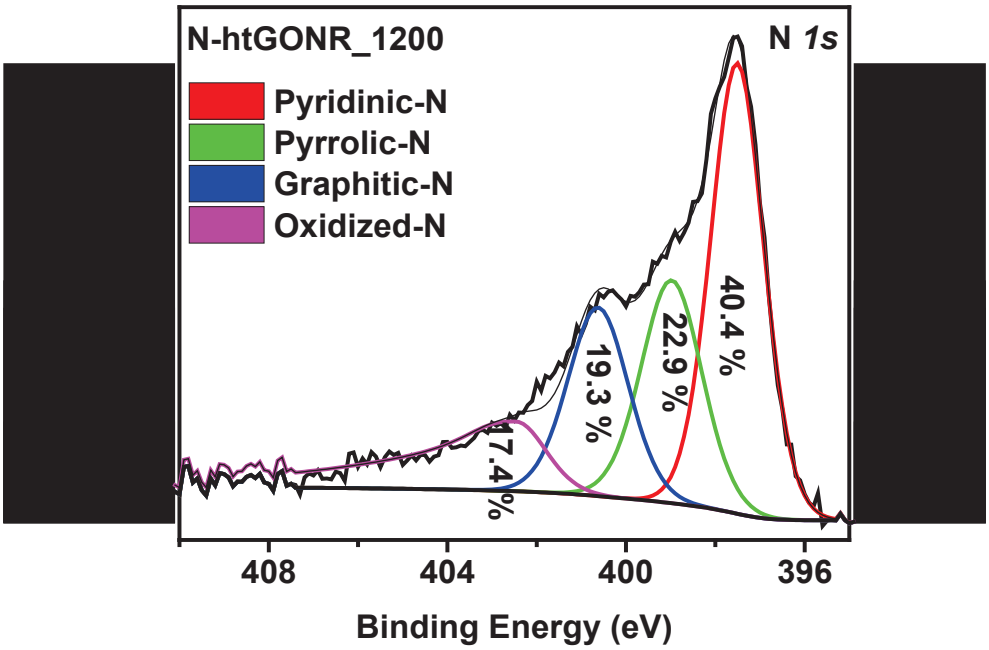

Figure 25: Example of deconvoluted N 1s peak in XPS spectra of nitrogen-doped heat-treated graphene oxide.

Exercise 2.1 (survey spectra)

1. Obtain the overview of XPS survey spectra of graphene derivatives in ASCI data format. The data can be exported to the Origin software, where peak analysis is performed. Select the exported data and click on the option at the top of the Origin software: Analysis/Peaks and Baseline/Peak Analyzer/Open dialog box. For a detailed analysis of peak deconvolution and integration, follow the link: https://www.youtube.com/watch?v=76F9QYp1pMk&t=124s&ab_channel=Nanoencryption

2. After peak integration, the elemental composition is determined by **Equation (19)**:

$$C_x = \frac{A_x/S_x}{\sum_i^n A_i/S_i} \tag{19}$$

where C_x is the fraction of element x, A_x is the peak area of element x, S_x is the relative sensitivity factor of photoelectron peak x (used to scale the measured peak areas so that variations in peak areas are representative of the amount of material on the sample surface). The S_x values used for the calculation are $S_{C\ 1s} = 1$, $S_{N\ 1s} = 1.8$, and $S_{O\ 1s} = 2.93$.

Exercise 2.2 (high-resolution spectra)

1. Obtain high-resolution N *1s* peak from XPS spectra in asci data format. The data can be exported to the Origin software, where peak deconvolution is performed. Select the exported data and click the option at the top of the Origin software: Analysis/Peaks and Baseline/Peak Analyzer/Open dialog box. For a detailed analysis of peak deconvolution and integration, follow the link:

https://www.youtube.com/watch?v=76F9QYp1pMk&t=124s&ab_channel=Nanoencryption

For the binding energies constraint, use the following intervals: 397.7 – 397.4 eV (pyridine-N), 398.7 – 399.0 eV (pyrrole-N), 400.2 – 400.6 eV (graphite-N), and 402.4 – 402.8 eV (oxidized-N). For the FWHM (full width at half maximum of the peak) constraint, use 1.2 – 1.6.

2. After peak integration, the configuration type is determined by **Equation (20)**:

$$N_x = \frac{A_x}{\sum_i^n A_i} \tag{20}$$

where N_x is the configuration type of N in at.%.

Questions

1. Which C *1s* electron is likely to have a higher *BE* -**C**OOH or -**C**H_2-OH? Why?

2. Why are the measurements carried out in a vacuum?

3. Can we measure non-conducting materials with XPS?

4. What is the physical meaning of the ionization cross-section, and why can hydrogen and helium peaks not be detected with XPS?

5. The XPS spectra for the concentrations of C, N, and O from **Exercise 2.1** are based on the number of atoms percentage (in at.%). Convert them to the mass percentage (assuming that only C, N, and O atoms are present in the sample).

3.3. Thermal analysis (TA)

Thermal analysis (TA) generally involves methods that measure physical (evaporation, sublimation, adsorption, desorption, crystalline transition, melting) and chemical (desolvation, chemisorption, decomposition, solid-gas reactions) changes in a material as a function of increasing temperature or at a constant temperature. There are three main TA methods: (i) thermogravimetric analysis (TGA), which measures the change in sample weight; (ii) differential scanning calorimetry (DSC), which measures the amount of heat required to keep the reference and sample at the same temperature; and (iii) differential thermal analysis (DTA), which measures the temperature difference between the reference and sample.[91]

As shown in **Figure 26**, the TA instrumentation consists of a highly sensitive balance connected to a sample holder in a furnace. Depending on the type of TA, the sample holder consists of various crucible holders connected to the balance while the sample is heated in a closed, temperature-programmed furnace.[92]

To obtain reproducible measurements and to exclude artifacts affecting the mass change (air buoyancy, convection inside the furnace, crucible geometry, radiation effects, atmosphere), a baseline correction is performed before the sample measurement. The baseline correction is performed by exposing the empty sample holder to the same parameters used for sample analysis.[91]

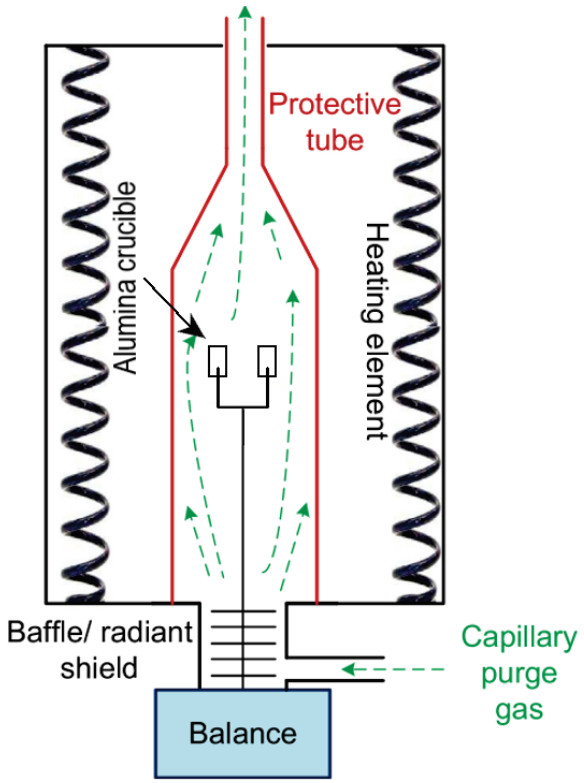

Figure 26: Schematic representation of the TGA/DTA instrumentation.[92]

In the case of graphene oxide derivatives, despite the study of thermal stability,[93] one of the factors that influence the properties, subsequent modification, and degree of exfoliation is the amount of oxygen present in the structure.[94] One of the methods that can be used to determine the oxygen concentration is TGA in conjunction with mass spectroscopy (MS). It should be noted that the determination of the amount of oxygen is based on the thermostability of the oxygen groups; therefore, the thermally stable oxygen cannot be quantified as a function of the final temperature. The standard TGA mass loss of graphene oxide below 150 °C is due to physically adsorbed water, between 150 °C – 250 °C is due to chemically adsorbed water, and at higher temperatures, the mass loss is due to decomposition of the oxygen functional groups.[92]

Exercise 3

Obtain TA-QMS (quadrupole analyzer mass spectroscope) plots of graphene oxide derivative.

a) From the TGA plot, determine the percentage of mass loss during the process. How much of the mass loss is due to the physisorption of water?

b) Using the QMS(T) plot, identify the major mass fragments during the TA. Why is carbon also present in some fragments?

Questions

1. Name three physical and three chemical material changes that can be observed during thermal analysis. Which processes are not detected by TGA but are detected by DSC or DTA?

2. What type of thermal analysis (DSC or DTA) did we use? What do they measure? What is the main difference between them?

3. What materials are used for the sample holders?

4. What would be left if graphene oxide was heated in an oxidizing atmosphere?

3.4. Brunauer-Emmett-Teller (BET) surface analysis

The most common method for determining surface efficiency, pore size distribution, and qualitative determination of the number of graphene layers is non-destructive BET surface analysis. The ideal single-layer graphene has a theoretical surface area of 2630 m^2/g, but the actual surface area of graphene derivatives is usually much smaller due to the spontaneous agglomeration, stacking, and overlapping of exfoliated sheets of graphene derivatives.[95]

The BET theory aims to explain the multilayer physical adsorption of chemically inert gas molecules (adsorbent) on a solid surface (adsorbate). The main concepts of the theory are the following: gas molecules can physically adsorb to a solid in an infinite number of layers; gas molecules can only interact with adjacent layers using the laws of Langmuir theory; the enthalpy of adsorption for the first layer is the highest and decreases with each subsequent layer until it remains a constant value at the enthalpy of liquefaction. The resulting equation is:[95,96]

$$v = \frac{v_{\mathrm{m}} c p}{(p_0 - p)(p_0 + p(c-1))} \tag{21}$$

where p and p_0 are the equilibrium and the saturated pressure of the adsorbates at the adsorption temperature, respectively, c is the constant BET, v is the total volume of adsorbed gas, and v_{m} is the volume of adsorbed gas when the entire adsorbent surface is covered with a complete unimolecular layer.[95]

Equation (21) can be reformulated as follows:

$$\frac{p}{v(p_0 - p)} = \frac{1}{v_{\mathrm{m}} c} + \frac{c-1}{v_{\mathrm{m}} c} \frac{p}{p_0} \tag{22}$$

If one plots $p/v(p_0 - p)$ against p/p_0 at low values ($0.05 < p/p_0 < 0.35$), one obtains the slope $(c - 1)/v_{\mathrm{m}}c$ and the intercept $1/v_{\mathrm{m}}c$. We can then determine c and v_{m} from the slope and intercept. The BET surface area can then be calculated as follows:[95]

$$S_{\mathrm{BET}} = \frac{v_{\mathrm{m}} N_{\mathrm{A}} s}{V_{\mathrm{M}} m} \tag{23}$$

where S_{BET} is the BET surface area, N_A is the Avogadro number, s is the adsorption cross-section of the adsorbed molecule, V_M is the molar volume of the adsorbed gas, and m is the mass of the adsorbate.[95]

The instrumentation records various pressures of the gas in the sample cell at constant temperature and calculates the amount of gas adsorbed/desorbed (at standard temperature and pressure). This is done using the manometer, which measures the amount of gas removed from the gas phase. Since the model BET measures the *relative pressure* of the adsorbing gas molecules, the gas must be condensable on the adsorbate at the adsorption temperature (for N_2, this is achieved by a liquid N_2 cold trap). At constant temperature, a known amount of pure gas (adsorbate) is allowed to enter the sample cell. During adsorption, the pressure in the enclosed volume decreases until equilibrium is reached. The amount of gas adsorbed at equilibrium pressure is the difference between the amount of gas admitted and the dead volume (previously determined by the admitted gas being negligibly adsorbed onto the adsorbent). The measurement continues with the successive point-by-point addition of gas to the absorbent. All the pressures measured are shown in relation to p_0, which is measured in an empty glass tube at the beginning or determined simultaneously with the measurement in a second tube.[97,98]

The main stages of the BET surface analysis procedure are shown schematically in **Figure 27**. First (step 1), the weight of the sample in the glass tube is measured. Then, this is repeated after degassing and evacuation (step 2). Next, we place the glass tube above the liquid N_2 cold trap. The instrument then lowers the glass into the N_2 cold trap when the dead volume has been measured (step 3). In step 4, the glass tube is raised out of the cold trap, where the gas is evacuated. Finally, the glass tube is lowered back into the cold trap, and the physisorption isotherm is measured when N_2 gas is added or removed (steps 5 and 6).[96]

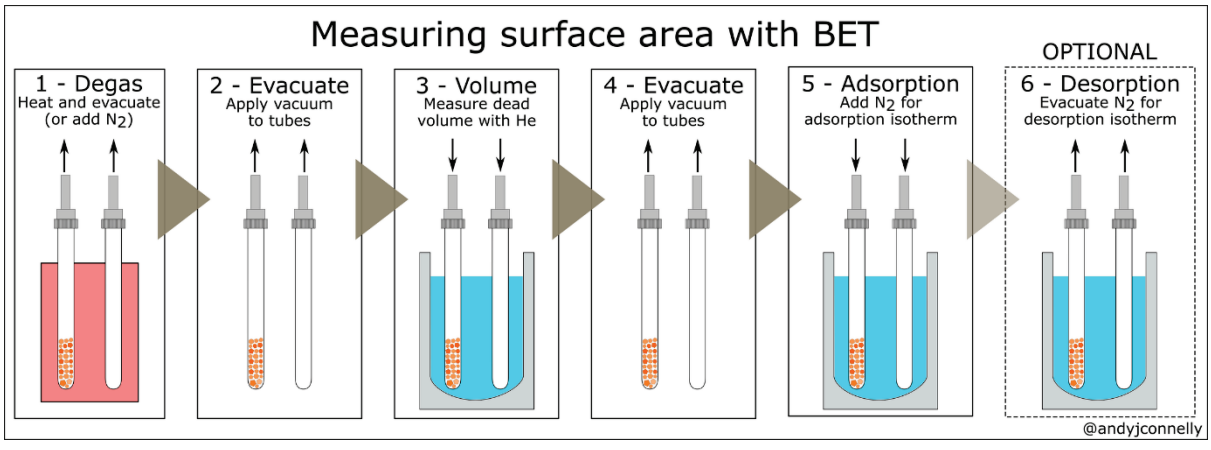

Figure 27: Various steps during the surface area with the BET measurment.[98]

Exercise 4

1. Using the data provided, create a BET graph of the measured graphene derivative.

2. Calculate the BET surface area using the **equations (22)** and **(23)** ($s(N_2)$ = 0.162 nm).

   S_{BET} =

Questions

1. The theoretical calculations show that the largest surface area of single-layer graphene is 2630 m²/g. Why is the BET-specific surface area of the measured graphene derivative lower than the theoretical predictions?

2. Calculate the theoretical surface area of single-layer graphene ($d_{C\text{-}C}$ = 0.142 nm, the hexagonal graphene lattice consists of two carbon atoms, N_A = 6.022 10^{23} mol^{-1}, M(C) = 12 g/mol).

3.5. Inductively coupled plasma mass spectroscopy (ICP-MS)

Due to the large specific surface area and the synthesis process involving starting materials, other precursors, and solvents with inherent metal impurities, graphene derivatives usually contain significant concentrations of metals (Fe, Mn, Co, Ni, Cu, etc.). These impurities are adsorbed from the reaction mixtures on the surface and can affect the electrocatalytic properties at concentrations as low as a few ppm, leading to misinterpretation of the electrochemical data.[99,100,101,102,103,104,105]

The use of conventional analytical methods (EDS, XAS, XPS, etc.) to determine the elemental concentration of graphene derivatives is unsuitable for the determination of trace metal impurities because of the high detection limits. Therefore, for the characterization of trace metals, we need to use instruments with higher detection limits, such as inductively coupled plasma mass spectrometry/optical emission spectroscopy (ICP MS), inductively coupled plasma optical emission spectroscopy (ICP OES), nuclear activation analysis (NAA), or X-ray fluorescence.[81]

We will focus here on the ICP-MS method. The determination of elemental impurities in graphene derivatives is not a simple task; the main problem is the sample preparation step. Due to the stable structure of graphene derivatives, it is extremely difficult to digest them into the solution. Therefore, not all metals are extracted from the material into the solution utilizing traditional digestion methods.[106] The method used for sample preparation consists of microwave-assisted acid digestion in three temperature steps with the use of highly purified acids H_2SO_4, $HClO_4$, and HNO_3.

In the next step, the sample is converted into an aerosol by nebulizer (shown in **Figure 28**) or vaporized by laser ablation or electrothermal evaporation and passed into the ICP with the carrier gas current. In the ICP, atomic excitation of the sample takes place. This is done by high-temperature plasma (up to 10000 K at the edges) generated by inelastic interaction between electrons and carrier gas (typically Ar gas) in the magnetic field. If the electrons have sufficient kinetic energy, they can eject the electron upon collision with carrier gas atoms. The newly formed electrons then accelerate again, and the process continues until there is equilibrium between the electron ejection and the recombination rate of the electron-gas ions (Ar^+ ions and electrons from Ar).[105] Ions and electrons interact with the fluctuating magnetic field, resulting in a closed ring-shaped flux through the induction coil. Ohmic heat is generated in response to the resistance exerted by the motion through the magnetic field.[105,82]

Subsequently, the ions formed during ICP are passed to the mass analyzer (electrostatic-magnetic, quadrupole, ion trap, time-of-flight, etc.), where the ions are separated based on their mass-to-charge ratio, and finally to the MS detector. The concentration of the detected atoms is determined by calibration with a suitable standard.[105]

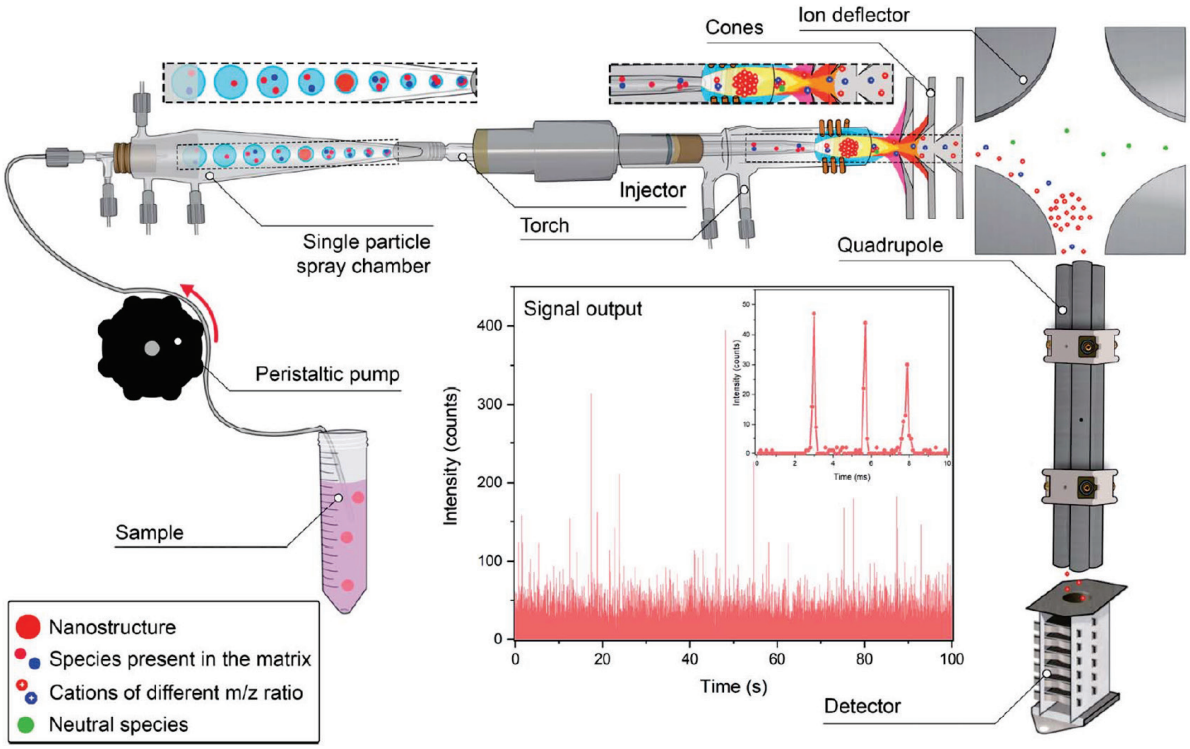

Figure 28: Schematically presented ICP-MS instrumentation.[107]

Procedure:

Microwave-assisted acid digestion: Weigh 30 mg of a graphene derivative into a clean vessel. Then, slowly add 5 mL of H_2SO_4 (96 wt.%), 3 mL of HNO_3 (65 wt.%), and 2 mL of $HClO_4$ (70 wt.%) to the autoclave. Close the autoclave and place it in the microwave. Use the following temperature program in **Table 1**. In addition to the sample, prepare the blank sample (using the same procedure without the graphene derivative). After the program is completed, dilute the blank solution and the graphene derivative by factors of 10 and 100 with a 1% HNO_3 solution.

Table 2: Temperature program for microwave-assisted acid digestion.

Step	Ramp time [min]	T [°C]	Hold time [min]
1	15	150	15
2	10	220	20
3	5	230	15

Preparation of standard solutions:

Approximately 50 mg of the catalyst powder was placed into 50 mL autoclave and added 4 mL H_2SO_4 (96 wt.%, Fluka-Honeywell, puriss), 3 mL HNO_3 (65 wt.%, Merck, suprapur), 2 mL $HClO_4$ (70 wt.%, Merck, suprapur), and 1 mL HF (40 wt.%, Merck, suprapur). The mixture

was heated according to the temperature program: to 150 °C for 15 min, 220 for 20 min, 230 for 15 min, and left to cool down in a microwave digestion system (Milestone Ethos UP). Next, the mixture was transferred to a 50 mL flask and diluted to the mark with ultrapure water. Finally, the as-prepared solution was filtrated through a 0.45 μm filter, diluted by factor 100 with 1 wt,% HNO_3 (65 wt.%, Merck, suprapur) solution, and injected into ICP-MS instrumentation.

ICP-MS analysis:

Trace element analysis of electrocatalysts was determined using an ICP-MS Agilent Technologies 7900CE, with a micro nebulizer, quartz spray chamber, and quadrupole mass analyzer in the flow of high-purity argon (5.0) gas at a flow rate of 15 L/min. The data were processed and analyzed using MassHunter 4.4. software.

Exercise 5

Calculate the concentrations of impurities (Fe, Mn, and K) by comparing the area and concentration between the standard and sample peaks. The area of the blank sample should be subtracted from all peaks. Report the results as a mass fraction (w) in parts per million (ppm).

w(Fe) = w(Mn) = w(K) =

Questions

1. What is plasma? Why are gases with high ionization energy used as carrier gases?

2. Why is the plasma generated by ICP the hottest at the edges of the cylindrical coil?

3. What is the main source of impurity?

4. How the impurities should be removed?

3.6. Scanning electron microscopy (SEM)

The development of SEM represented a breakthrough in the study of the microstructure, composition, and properties of bulk materials. The electrons used in SEM can be extracted from various filaments by resistive heating (typically W due to the high melting point and low vapor pressure). Their velocity and, hence, energy can be easily controlled by the electrostatic fields; by using magnetic and electrostatic lenses, we can shape them into a finely focused beam that is scanned over a surface of interest. When these electrons, also called "primary electrons", interact with matter, they produce a variety of charged particles and photons (as seen in **Figure 29**) that can be used to characterize topography, composition, and bulk material properties.[108]

The shorter the wavelength of the radiation, the higher the magnification. In optical microscopes, wavelengths of 550 nm are used, while SEM 1–10 nm at an electron energy of 30 kV–100 kV. Therefore, another advantageous property of SEM is the magnification (features smaller than 1 nm can be detected).[108]

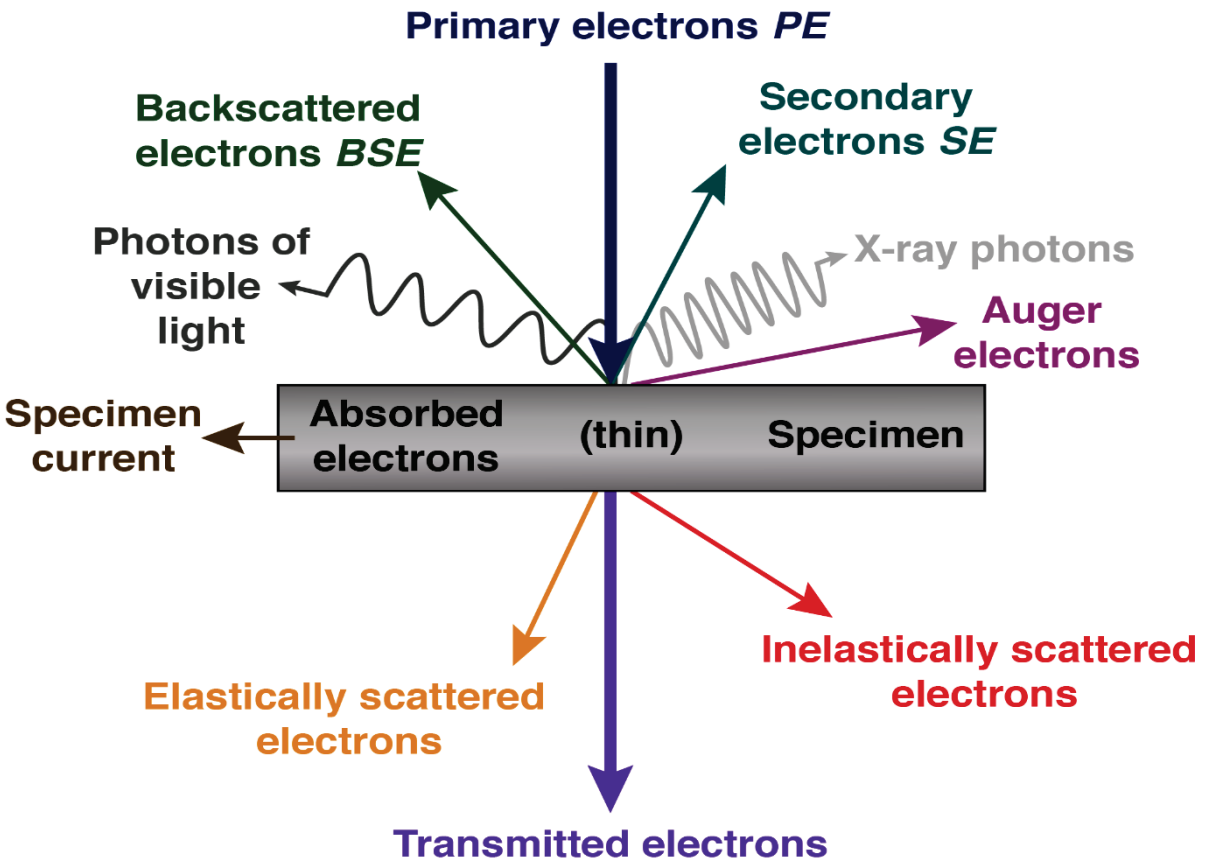

Figure 29: Possible different signals produced by the interaction of primary electrons and matter. For a sample that is more than a few hundred nanometers thick, the electrons are absorbed and, therefore, not transmitted.

In morphology imaging, the main charged particles are secondary electrons and backscattered (less frequently used due to their penetration depth). Secondary electrons are electrons produced by the ionization of primary electrons, and backscattered electrons are primary electrons that are deflected by collisions with atoms of matter to such an extent that they are carried back up through the sample surface. The varying composition of the surface topography affects the generation, transport, and escape of these signals. From the variations in the intensity of the electron signals detected at each point on the sample scanned by the electron beam, the image is formed.[80,108]

The chemical composition of matter in the SEM is most commonly determined by X-rays using energy-dispersive X-ray spectroscopy (EDS). Here, the X-rays are emitted due to the relaxation of the atom in the excited state caused by the primary electron. These important species are emitted because of the relaxation of an excited state in an atom. The first excited state is caused by the ionization of a tightly bound inner electron by an incident primary electron.[80,108]

For the SEM measurements, three conditions must be met. First, a high-vacuum (10^{-3} – 10^{-5} Pa) must exist in the sample chamber to minimize primary electron scattering and contamination of the electron source; second, the sample should be electrically conductive. Therefore, the sample should be conductive or made conductive by sputter-coating with conductive material (Au, Pt, Pd, Cr, etc.); third, the molar mass for the standard SEM instrumentation must be higher than 4 for EDS to detect the signal.[108,109]

We will characterize the graphene derivatives prepared by CVD and top-down synthesis using SEM imaging and EDS elemental characterization.

Procedure

Cover the top of the conducting carbon type on the aluminum SEM holder with the bulk graphene derivative or with the CVD-grown graphene electrode. (All samples are good conductors, so sputter-coating is not required.) The SEM and EDS measurements will be performed by a trained, qualified person.

Exercise 6

Describe the morphology of CVD-grown graphene and bulk graphene derivatives. For CVD-grown graphene, also determine the density of graphene domains**.**

Compare the elemental composition results between the XPS and EDS methods. Discuss the results.

Questions

1. Why does the sample need to be conductive SEM imaging?

2. What are the differences between EDS and XPS?

3. Why do some parts of the SEM images change from dark to bright during the measurement?

Literature

(1) Higgins, D.; Zamani, P.; Yu, A.; Chen, Z. The Application of Graphene and Its Composites in Oxygen Reduction Electrocatalysis: A Perspective and Review of Recent Progress. *Energy Environ Sci* **2016**, *9* (2), 357–390. https://doi.org/10.1039/c5ee02474a.

(2) Owusu, P. A.; Asumadu-Sarkodie, S. A Review of Renewable Energy Sources, Sustainability Issues and Climate Change Mitigation. *Cogent Eng* **2016**, *3* (1), 1–14. https://doi.org/10.1080/23311916.2016.1167990.

(3) Nie, Y.; Li, L.; Wei, Z. Recent Advancements in Pt and Pt-Free Catalysts for Oxygen Reduction Reaction. *Chem Soc Rev* **2015**, *44* (8), 2168–2201. https://doi.org/10.1039/c4cs00484a.

(4) Fan, L.; Tu, Z.; Chan, S. H. Recent Development of Hydrogen and Fuel Cell Technologies: A Review. *Energy Reports* **2021**, *7*, 8421–8446. https://doi.org/10.1016/j.egyr.2021.08.003.

(5) Sharaf, O. Z.; Orhan, M. F. An Overview of Fuel Cell Technology: Fundamentals and Applications. *Renewable and Sustainable Energy Reviews* **2014**, *32*, 810–853. https://doi.org/10.1016/j.rser.2014.01.012.

(6) Ragupathy, P.; Bhat, S. D.; Kalaiselvi, N. Electrochemical Energy Storage and Conversion: An Overview. *Wiley Interdiscip Rev Energy Environ* **2023**, *12* (2), 1–29. https://doi.org/10.1002/wene.464.

(7) Liu, Y.; Wu, Q.; Liu, L.; Manasa, P.; Kang, L.; Ran, F. Vanadium Nitride for Aqueous Supercapacitors: A Topic Review. *J Mater Chem A Mater* **2020**, *8* (17), 8218–8233. https://doi.org/10.1039/d0ta01490g.

(8) *Proton-exchange membrane fuel cell*. https://en.wikipedia.org/wiki/Proton-exchange_membrane_fuel_cell.

(9) Wang, Y.; Chen, K. S.; Mishler, J.; Cho, S. C.; Adroher, X. C. A Review of Polymer Electrolyte Membrane Fuel Cells: Technology, Applications, and Needs on Fundamental Research. *Appl Energy* **2011**, *88* (4), 981–1007. https://doi.org/10.1016/j.apenergy.2010.09.030.

(10) Park, K. W.; Choi, J. H.; Kwon, B. K.; Lee, S. A.; Sung, Y. E.; Ha, H. Y.; Hong, S. A.; Kim, H.; Wieckowski, A. Chemical and Electronic Effects of Ni in Pt/Ni and Pt/Ru/Ni Alloy Nanoparticles in Methanol Electrooxidation. *Journal of Physical Chemistry B* **2002**, *106* (8), 1869–1877. https://doi.org/10.1021/jp013168v.

(11) Kirubakaran, A.; Jain, S.; Nema, R. K. A Review on Fuel Cell Technologies and Power Electronic Interface. *Renewable and Sustainable Energy Reviews* **2009**, *13* (9), 2430–2440. https://doi.org/10.1016/j.rser.2009.04.004.

(12) Pandey, R.; Agarwal, H.; Saravanan, B.; Sridhar, P.; Bhat, S. D. Internal Humidification in PEM Fuel Cells Using Wick Based Water Transport. *J Electrochem Soc* **2015**, *162* (9), F1000–F1010. https://doi.org/10.1149/2.0621509jes.

(13) Larminie, J.; Dicks, A. *Fuel Cell Systems Explained*; 2003. https://doi.org/10.1002/9781118878330.

(14) Jung, J. H.; Ahmed, S. Dynamic Model of PEM Fuel Cell Using Real-Time Simulation Techniques. *Journal of Power Electronics* **2010**, *10* (6), 739–748. https://doi.org/10.6113/JPE.2010.10.6.739.

(15) Francesco Valle. Electrocatalyst Degradation in High Temperature PEM Fuel Cells. PhD, UNIVERSITÀ DEGLI STUDI DI TRIESTE, TRIESTE, 2015.

(16) Guo, S.; Sun, S. FePt Nanoparticles Assembled on Graphene as Enhanced Catalyst for Oxygen Reduction Reaction. *J Am Chem Soc* **2012**, *134* (5), 2492–2495. https://doi.org/10.1021/ja2104334.

(17) Jaouen, F.; Proietti, E.; Lefèvre, M.; Chenitz, R.; Dodelet, J. P.; Wu, G.; Chung, H. T.; Johnston, C. M.; Zelenay, P. Recent Advances in Non-Precious Metal Catalysis for Oxygen-Reduction Reaction in Polymer Electrolyte Fuel Cells. *Energy Environ Sci* **2011**, *4* (1), 114–130. https://doi.org/10.1039/c0ee00011f.

(18) Liu, M.; Wang, L.; Zhao, K.; Shi, S.; Shao, Q.; Zhang, L.; Sun, X.; Zhao, Y.; Zhang, J. Atomically Dispersed Metal Catalysts for the Oxygen Reduction Reaction: Synthesis, Characterization, Reaction Mechanisms and Electrochemical Energy Applications. *Energy Environ Sci* **2019**, *12* (10), 2890–2923. https://doi.org/10.1039/c9ee01722d.

(19) Sui, S.; Wang, X.; Zhou, X.; Su, Y.; Riffat, S.; Liu, C. jun. A Comprehensive Review of Pt Electrocatalysts for the Oxygen Reduction Reaction: Nanostructure, Activity, Mechanism and Carbon Support in PEM Fuel Cells. *J Mater Chem A Mater* **2017**, *5* (5), 1808–1825. https://doi.org/10.1039/C6TA08580F.

(20) Chen, D.; Tao, Q.; Liao, L. W. Determining the Active Surface Area for Various Platinum Electrodes Determining the Active Surface Area for Various Platinum Electrodes. **2011**, No. September. https://doi.org/10.1007/s12678-011-0054-1.

(21) Mahata, A.; Nair, A. S.; Pathak, B. Recent Advancements in Pt-Nanostructure-Based Electrocatalysts for the Oxygen Reduction Reaction. *Catal Sci Technol* **2019**, *9* (18), 4835–4863. https://doi.org/10.1039/c9cy00895k.

(22) Jean Moriau, L.; Hrnji, A.; Pavli si, A.; Rebeka Kam sek, A.; sa Petek, U.; Ruiz-Zepeda, F.; Sala, M.; Pavko, L.; Simon Selih, V.; Bele, M.; Jovanovi, P.; Gatalo, M.; Hodnik, N. IScience Resolving the Nanoparticles' Structure-Property Relationships at the Atomic Level: A Study of Pt-Based Electrocatalysts. https://doi.org/10.1016/j.isci.

(23) Greeley, J.; Stephens, I. E. L.; Bondarenko, A. S.; Johansson, T. P.; Hansen, H. A.; Jaramillo, T. F.; Rossmeisl, J.; Chorkendorff, I.; Nørskov, J. K. Alloys of Platinum and Early Transition Metals as Oxygen Reduction Electrocatalysts. *Nat Chem* **2009**, *1* (7), 552–556. https://doi.org/10.1038/nchem.367.

(24) Zhang, J.; Vukmirovic, M. B.; Xu, Y.; Mavrikakis, M.; Adzic, R. R. Controlling the Catalytic Activity of Platinum-Monolayer Electrocatalysts for Oxygen Reduction with Different Substrates. *Angewandte Chemie* **2005**, *117* (14), 2170–2173. https://doi.org/10.1002/ange.200462335.

(25) Bele, M.; Jovanovič, P.; Pavlišič, A.; Jozinović, B.; Zorko, M.; Rečnik, A.; Chernyshova, E.; Hočevar, S.; Hodnik, N.; Gaberšček, M. A Highly Active PtCu3 Intermetallic Core–Shell, Multilayered Pt-Skin, Carbon Embedded Electrocatalyst Produced by a Scale-up Sol–Gel

Synthesis. *Chemical Communications* **2014**, *50* (86), 13124–13126. https://doi.org/10.1039/c4cc05637j.

(26) Pavko, L.; Gatalo, M.; Đukić, T.; Ruiz-Zepeda, F.; Surca, A. K.; Šala, M.; Maselj, N.; Jovanovič, P.; Bele, M.; Finšgar, M.; Genorio, B.; Hodnik, N.; Gaberšček, M. Correlating Oxygen Functionalities and Electrochemical Durability of Carbon Supports for Electrocatalysts. *Carbon N Y* **2023**, *215*. https://doi.org/10.1016/j.carbon.2023.118458.

(27) Liu, L.; Corma, A. Metal Catalysts for Heterogeneous Catalysis: From Single Atoms to Nanoclusters and Nanoparticles. *Chem Rev* **2018**, *118* (10), 4981–5079. https://doi.org/10.1021/acs.chemrev.7b00776.

(28) Georgakilas, V.; Perman, J. A.; Tucek, J.; Zboril, R. Broad Family of Carbon Nanoallotropes: Classification, Chemistry, and Applications of Fullerenes, Carbon Dots, Nanotubes, Graphene, Nanodiamonds, and Combined Superstructures. *Chem Rev* **2015**, *115* (11), 4744–4822. https://doi.org/10.1021/cr500304f.

(29) Genorio, B.; Harrison, K. L.; Connell, J. G.; Dražić, G.; Zavadil, K. R.; Markovic, N. M.; Strmcnik, D. Tuning the Selectivity and Activity of Electrochemical Interfaces with Defective Graphene Oxide and Reduced Graphene Oxide. *ACS Appl Mater Interfaces* **2019**, *11* (37), 34517–34525. https://doi.org/10.1021/acsami.9b13391.

(30) Kim, H.; Lee, K.; Woo, S. I.; Jung, Y. On the Mechanism of Enhanced Oxygen Reduction Reaction in Nitrogen-Doped Graphene Nanoribbons. *Physical Chemistry Chemical Physics* **2011**, *13* (39), 17505–17510. https://doi.org/10.1039/c1cp21665a.

(31) Shen, A.; Zou, Y.; Wang, Q.; Dryfe, R. A. W.; Huang, X.; Dou, S.; Dai, L.; Wang, S. Oxygen Reduction Reaction in a Droplet on Graphite: Direct Evidence That the Edge Is More Active than the Basal Plane. *Angewandte Chemie - International Edition* **2014**, *53* (40), 10804–10808. https://doi.org/10.1002/anie.201406695.

(32) Nosan, M.; Löffler, M.; Jerman, I.; Kolar, M.; Katsounaros, I.; Genorio, B. Understanding the Oxygen Reduction Reaction Activity of Quasi-1D and 2D N-Doped Heat-Treated Graphene Oxide Catalysts with Inherent Metal Impurities. *ACS Appl Energy Mater* **2021**. https://doi.org/10.1021/acsaem.1c00026.

(33) Higgins, D.; Zamani, P.; Yu, A.; Chen, Z. The Application of Graphene and Its Composites in Oxygen Reduction Electrocatalysis: A Perspective and Review of Recent Progress. *Energy Environ Sci* **2016**, *9* (2), 357–390. https://doi.org/10.1039/c5ee02474a.

(34) Jariwala, D.; Srivastava, A.; Ajayan, P. M. Graphene Synthesis and Band Gap Opening. *J Nanosci Nanotechnol* **2011**, *11* (8), 6621–6641. https://doi.org/10.1166/jnn.2011.5001.

(35) Higginbotham, A. L.; Lomeda, J. R.; Morgan, A. B.; Tour, J. M. Graphite Oxide Flame-Retardant Polymer Nanocomposites. *ACS Appl Mater Interfaces* **2009**, *1* (10), 2256–2261. https://doi.org/10.1021/am900419m.

(36) Dimiev, A. M.; Tour, J. M.; Science, M.; Science, C.; Science, N.; Street, M.; States, U.; Materials, A. Z. E.; Avenue, M.; States, U. Terms of Use Mechanism of Graphene Oxide. *ACS Nano* **2014**, *8* (3), 3060–3068. https://doi.org/10.1021/nn500606a.

(37) Marcano, D. C.; Kosynkin, D. V; Berlin, J. M.; Sinitskii, A.; Sun, Z.; Slesarev, A. S.; Alemany, L. B.; Lu, W.; Tour, J. M. Correction to: Improved Synthesis of Graphene Oxide. *ACS Nano* **2018**, *12* (2), 2078. https://doi.org/10.1021/acsnano.8b00128.

(38) Lu, Z. J.; Bao, S. J.; Gou, Y. T.; Cai, C. J.; Ji, C. C.; Xu, M. W.; Song, J.; Wang, R. Nitrogen-Doped Reduced-Graphene Oxide as an Efficient Metal-Free Electrocatalyst for Oxygen Reduction in Fuel Cells. *RSC Adv* **2013**, *3* (12), 3990–3995. https://doi.org/10.1039/c3ra22161j.

(39) Yadav, R.; Dixit, C. K. Synthesis, Characterization and Prospective Applications of Nitrogen-Doped Graphene: A Short Review. *Journal of Science: Advanced Materials and Devices* **2017**, *2* (2), 141–149. https://doi.org/10.1016/j.jsamd.2017.05.007.

(40) Inagaki, M.; Toyoda, M.; Soneda, Y.; Morishita, T. Nitrogen-Doped Carbon Materials. *Carbon N Y* **2018**, *132*, 104–140. https://doi.org/10.1016/j.carbon.2018.02.024.

(41) Xu, H.; Ma, L.; Jin, Z. Nitrogen-Doped Graphene: Synthesis, Characterizations and Energy Applications. *Journal of Energy Chemistry* **2018**, *27* (1), 146–160. https://doi.org/10.1016/j.jechem.2017.12.006.

(42) Vashisth, A.; Upama, S. T.; Anas, M.; Oh, J.-H.; Patil, N.; Green, M. J. Radio Frequency Heating and Material Processing Using Carbon Susceptors. *Nanoscale Adv* **2021**. https://doi.org/10.1039/D1NA00217A.

(43) Wyss, K. M.; Beckham, J. L.; Chen, W.; Xuan Luong, D.; Hundi, P.; Raghuraman, S.; Shahsavari, R.; Tour, J. M. *Converting Plastic Waste Pyrolysis Ash into Flash Graphene*; 2021.

(44) Advincula, P. A.; Granja, V.; Wyss, K. M.; Algozeeb, W. A.; Chen, W.; Beckham, J. L.; Luong, D. X.; Higgs, C. F.; Tour, J. M. Waste Plastic- and Coke-Derived Flash Graphene as Lubricant Additives. *Carbon N Y* **2023**, *203*, 876–885. https://doi.org/10.1016/j.carbon.2022.12.035.

(45) Wyss, K. M.; Luong, D. X.; Tour, J. M. Large-Scale Syntheses of 2D Materials: Flash Joule Heating and Other Methods. *Advanced Materials*. John Wiley and Sons Inc February 1, 2022. https://doi.org/10.1002/adma.202106970.

(46) Sattari, K.; Eddy, L.; Beckham, J. L.; Wyss, K. M.; Byfield, R.; Qian, L.; Tour, J. M.; Lin, J. A Scientific Machine Learning Framework to Understand Flash Graphene Synthesis. *Digital Discovery* **2023**, *2* (4), 1209–1218. https://doi.org/10.1039/d3dd00055a.

(47) Luong, D. X.; Bets, K. V.; Algozeeb, W. A.; Stanford, M. G.; Kittrell, C.; Chen, W.; Salvatierra, R. V.; Ren, M.; McHugh, E. A.; Advincula, P. A.; Wang, Z.; Bhatt, M.; Guo, H.; Mancevski, V.; Shahsavari, R.; Yakobson, B. I.; Tour, J. M. Gram-Scale Bottom-up Flash Graphene Synthesis. *Nature* **2020**, *577* (7792), 647–651. https://doi.org/10.1038/s41586-020-1938-0.

(48) Jiang, Y.; Yang, L.; Sun, T.; Zhao, J.; Lyu, Z.; Zhuo, O.; Wang, X.; Wu, Q.; Ma, J.; Hu, Z. Significant Contribution of Intrinsic Carbon Defects to Oxygen Reduction Activity. *ACS Catal* **2015**, *5* (11), 6707–6712. https://doi.org/10.1021/acscatal.5b01835.

(49) Zhao, H.; Sun, C.; Jin, Z.; Wang, D. W.; Yan, X.; Chen, Z.; Zhu, G.; Yao, X. Carbon for the Oxygen Reduction Reaction: A Defect Mechanism. *J Mater Chem A Mater* **2015**, *3* (22), 11736–11739. https://doi.org/10.1039/c5ta02229k.

(50) Luo, Z.; Lim, S.; Tian, Z.; Shang, J.; Lai, L.; MacDonald, B.; Fu, C.; Shen, Z.; Yu, T.; Lin, J. Pyridinic N Doped Graphene: Synthesis, Electronic Structure, and Electrocatalytic Property. *J Mater Chem* **2011**, *21* (22), 8038–8044. https://doi.org/10.1039/c1jm10845j.

(51) Saeed, M.; Alshammari, Y.; Majee, S. A.; Al-Nasrallah, E. Chemical Vapour Deposition of Graphene—Synthesis, Characterisation, and Applications: A Review. *Molecules* **2020**, *25* (1–2), 50–61. https://doi.org/10.1016/S0040-6090(01)00814-8.

(52) Liu, X.; Dai, L. *Carbon-Based Metal-Free Catalysts*; 2016; Vol. 1. https://doi.org/10.1038/natrevmats.2016.64.

(53) Cai, W.; Zhao, X.; Liu, C.; Xing, W.; Zhang, J. *Electrode Kinetics of Electron-Transfer Reaction and Reactant Transport in Electrolyte Solution*; Elsevier B.V., 2014. https://doi.org/10.1016/B978-0-444-63278-4.00002-1.

(54) Du, C.; Tan, Q.; Yin, G.; Zhang, J. *Rotating Disk Electrode Method*; Elsevier B.V., 2014. https://doi.org/10.1016/B978-0-444-63278-4.00005-7.

(55) Jia, Z.; Yin, G.; Zhang, J. *Rotating Ring-Disk Electrode Method*; Elsevier B.V., 2014. https://doi.org/10.1016/B978-0-444-63278-4.00006-9.

(56) Zhou, R.; Zheng, Y.; Jaroniec, M.; Qiao, S. Z. Determination of the Electron Transfer Number for the Oxygen Reduction Reaction: From Theory to Experiment. *ACS Catal* **2016**, *6* (7), 4720–4728. https://doi.org/10.1021/acscatal.6b01581.

(57) Housecroft, C. E.; Sharpe, A. G. *Inorganic Chemistry, Fourth Edition*; 2012.

(58) Mayrhofer, K. J. J.; Wiberg, G. K. H.; Arenz, M. Impact of Glass Corrosion on the Electrocatalysis on Pt Electrodes in Alkaline Electrolyte. *J Electrochem Soc* **2008**, *155* (1), P1. https://doi.org/10.1149/1.2800752.

(59) Shinozaki, K.; Zack, J. W.; Pylypenko, S.; Pivovar, B. S.; Kocha, S. S. Oxygen Reduction Reaction Measurements on Platinum Electrocatalysts Utilizing Rotating Disk Electrode Technique II . Influence of Ink Formulation , Catalyst Layer Uniformity and Thickness. **2015**, *162* (12), 1384–1396. https://doi.org/10.1149/2.0551512jes.

(60) van der Heijden, O.; Park, S.; Eggebeen, J. J. J.; Koper, M. T. M. Non-Kinetic Effects Convolute Activity and Tafel Analysis for the Alkaline Oxygen Evolution Reaction on NiFeOOH Electrocatalysts. *Angewandte Chemie - International Edition* **2023**, *62* (7). https://doi.org/10.1002/anie.202216477.

(61) Metrohm-Autolab. Measuring Uncompensated Resistance on Micro-Electrodes Using Positive Feedback. *Autolab Application Note*.

(62) Area, A. Application Area : Fundamental Ohmic Drop Part 2 – Measurement. 2–5.

(63) Elezović, N. R.; Babić, B. M.; Vračar, L. J. M.; Krstajić, N. V. Oxygen Reduction at Platinum Nanoparticles Supported on Carbon Cryogel in Alkaline Solution. *Journal of the Serbian Chemical Society* **2007**, *72* (7), 699–708. https://doi.org/10.2298/JSC0707699E.

(64) Garsany, Y.; Ge, J.; St-Pierre, J.; Rocheleau, R.; Swider-Lyons, K. E. Analytical Procedure for Accurate Comparison of Rotating Disk Electrode Results for the Oxygen Reduction Activity of Pt/C. *J Electrochem Soc* **2014**, *161* (5), F628–F640. https://doi.org/10.1149/2.036405jes.

(65) Galeano, C.; Meier, J. C.; Soorholtz, M.; Bongard, H.; Baldizzone, C.; Mayrhofer, K. J. J.; Schüth, F. Nitrogen-Doped Hollow Carbon Spheres as a Support for Platinum-Based Electrocatalysts. *ACS Catalysis*. 2014, pp 3856–3868. https://doi.org/10.1021/cs5003492.

(66) Diaz-Morales, O.; Thomas, J. P. H.; Cansin, B.; Garcia C., A.; Koper, M. T. M. Hydrogen Adsorption on Nano-Structured Platinum Electrodes Oscar. *rsc* **2018**, 1–24. https://doi.org/10.1039/C8FD00062J.

(67) Shao, M.; Peles, A.; Shoemaker, K. Electrocatalysis on Platinum Nanoparticles : Particle Size Effect On. **2011**, 3714–3719.

(68) Pina, A.; Ferrão, P.; Fournier, J.; Lacarrière, B.; Corre, O. Le. Catalytic Activity of Various Platinum Loading in Acid Electrolyte at K the Heat Demand-Outdoor Assessing the Feasibility of Using Temperature Function for a Long-Term District Heat Demand Forecast. *Energy Procedia* **2017**, *138*, 229–234. https://doi.org/10.1016/j.egypro.2017.10.155.

(69) Gasteiger, H. A.; Kocha, S. S.; Sompalli, B.; Wagner, F. T. Activity Benchmarks and Requirements for Pt, Pt-Alloy, and Non-Pt Oxygen Reduction Catalysts for PEMFCs. *Appl Catal B* **2005**, *56* (1–2), 9–35. https://doi.org/10.1016/J.APCATB.2004.06.021.

(70) Malko, D.; Kucernak, A. Kinetic Isotope Effect in the Oxygen Reduction Reaction (ORR) over Fe-N/C Catalysts under Acidic and Alkaline Conditions. *Electrochem commun* **2017**, *83* (September), 67–71. https://doi.org/10.1016/j.elecom.2017.09.004.

(71) Garsany, Y.; Baturina, O. A.; Swider-Lyons, K. E.; Kocha, S. S. Experimental Methods for Quantifying the Activity of Platinum Electrocatalysts for the Oxygen Reduction Reaction. In *Analytical Chemistry*; 2010; Vol. 82, pp 6321–6328. https://doi.org/10.1021/ac100306c.

(72) Vazhayil, A.; Vazhayal, L.; Thomas, J.; Ashok C, S.; Thomas, N. A Comprehensive Review on the Recent Developments in Transition Metal-Based Electrocatalysts for Oxygen Evolution Reaction. *Applied Surface Science Advances* **2021**, *6*, 100184. https://doi.org/10.1016/J.APSADV.2021.100184.

(73) Liu, F.; Shi, C.; Guo, X.; He, Z.; Pan, L.; Huang, Z. F.; Zhang, X.; Zou, J. J. Rational Design of Better Hydrogen Evolution Electrocatalysts for Water Splitting: A Review. *Advanced Science*. John Wiley and Sons Inc June 1, 2022. https://doi.org/10.1002/advs.202200307.

(74) Mathew, M. M. Design of Nickel-Based Electrocatalysts for Electrochemical Production of H2, O2 and H2O2 in Alkaline and Neutral Media, University of Ljubljana, Ljubljana, 2023.

(75) Zheng, W. IR Compensation for Electrocatalysis Studies: Considerations and Recommendations. *ACS Energy Letters*. American Chemical Society April 14, 2023, pp 1952–1958. https://doi.org/10.1021/acsenergylett.3c00366.

(76) Lu, G.; Yang, H.; Zhu, Y.; Huggins, T.; Ren, Z. J.; Liu, Z.; Zhang, W. Synthesis of a Conjugated Porous Co(Ii) Porphyrinylene-Ethynylene Framework through Alkyne Metathesis and Its Catalytic Activity Study. *J Mater Chem A Mater* **2015**, *3* (9), 4954–4959. https://doi.org/10.1039/c4ta06231k.

(77) Zhao, H.; Sun, C.; Jin, Z.; Wang, D. W.; Yan, X.; Chen, Z.; Zhu, G.; Yao, X. Carbon for the Oxygen Reduction Reaction: A Defect Mechanism. *J Mater Chem A Mater* **2015**, *3* (22), 11736–11739. https://doi.org/10.1039/c5ta02229k.

(78) Yang, M.; Chen, H.; Yang, D.; Gao, Y.; Li, H. High-Performance Electrocatalyst for Oxygen Reduction Reaction Derived from Copolymer Networks and Iron(II) Acetate. *RSC Adv* **2016**, *6* (99), 97259–97265. https://doi.org/10.1039/c6ra24314b.

(79) Elezović, N. R.; Babić, B. M.; Vračar, L. J. M.; Krstajić, N. V. Oxygen Reduction at Platinum Nanoparticles Supported on Carbon Cryogel in Alkaline Solution. *Journal of the Serbian Chemical Society* **2007**, *72* (7), 699–708. https://doi.org/10.2298/JSC0707699E.

(80) Hu, M.; Yao, Z.; Wang, X. Characterization Techniques for Graphene-Based Materials in Catalysis. *AIMS Mater Sci* **2017**, *4* (3), 755–788. https://doi.org/10.3934/matersci.2017.3.755.

(81) Kiciński, W.; Dyjak, S. Transition Metal Impurities in Carbon-Based Materials: Pitfalls, Artifacts and Deleterious Effects. *Carbon N Y* **2020**, *168*, 748–845. https://doi.org/10.1016/j.carbon.2020.06.004.

(82) Skoog, D.; West, D. *Principles of Instrumental Analysis*, Second edi.; Saunders College: Philadelphia, 1980.

(83) Kumar, S.; Kumar, P.; Das, A.; Pathak, C. S. Surface-Enhanced Raman Scattering: Introduction and Applications. *Intech* **2016**, *i*, 13.

(84) Chaichi, A.; Prasad, A.; Ranjan Gartia, M. Raman Spectroscopy and Microscopy Applications in Cardiovascular Diseases: From Molecules to Organs. *Biosensors*. MDPI November 12, 2018. https://doi.org/10.3390/bios8040107.

(85) Wu, J. Bin; Lin, M. L.; Cong, X.; Liu, H. N.; Tan, P. H. Raman Spectroscopy of Graphene-Based Materials and Its Applications in Related Devices. *Chem Soc Rev* **2018**, *47* (5), 1822–1873. https://doi.org/10.1039/c6cs00915h.

(86) Childres, I.; Jauregui, L. A.; Park, W.; Caoa, H.; Chena, Y. P. Raman Spectroscopy of Graphene and Related Materials. *New Developments in Photon and Materials Research* **2013**, 403–418.

(87) Briggs, D. *X-Ray Photoelectron Spectroscopy (XPS)*; 2005. https://doi.org/10.1002/0470014229.ch22.

(88) Singh, S. K.; Takeyasu, K.; Nakamura, J. Active Sites and Mechanism of Oxygen Reduction Reaction Electrocatalysis on Nitrogen-Doped Carbon Materials. *Advanced Materials* **2019**, *31* (13), 1–17. https://doi.org/10.1002/adma.201804297.

(89) Shibuya, R.; Kondo, T.; Nakamura, J. Active Sites in Nitrogen-Doped Carbon Materials for Oxygen Reduction Reaction. *Carbon-Based Metal-Free Catalysts: Design and Applications* **2018**, *1–2* (6271), 227–249. https://doi.org/10.1002/9783527811458.vol1-ch8.

(90) Xing, T.; Zheng, Y.; Li, L. H.; Cowie, B. C. C.; Gunzelmann, D.; Qiao, S. Z.; Huang, S.; Chen, Y. Observation of Active Sites for Oxygen Reduction Reaction on Nitrogen-Doped Multilayer Graphene. *ACS Nano* **2014**, *8* (7), 6856–6862. https://doi.org/10.1021/nn501506p.

(91) Bottom, R. Thermogravimetric Analysis. *Principles and Applications of Thermal Analysis* **1963**, *1* (906), 87–118. https://doi.org/10.1002/9780470697702.ch3.

(92) Saadatkhah, N.; Carillo Garcia, A.; Ackermann, S.; Leclerc, P.; Latifi, M.; Samih, S.; Patience, G. S.; Chaouki, J. Experimental Methods in Chemical Engineering: Thermogravimetric Analysis—TGA. *Canadian Journal of Chemical Engineering* **2020**, *98* (1), 34–43. https://doi.org/10.1002/cjce.23673.

(93) Farivar, F.; Yap, P. L.; Karunagaran, R. U.; Losic, D. Effect of Particle Size of Graphene , Graphene Oxide and Graphite on Thermal Parameters. *Journal of Carbon Research* **2021**, *7*, 41.

(94) Youn, H. C.; Bak, S. M.; Kim, M. S.; Jaye, C.; Fischer, D. A.; Lee, C. W.; Yang, X. Q.; Roh, K. C.; Kim, K. B. High-Surface-Area Nitrogen-Doped Reduced Graphene Oxide for Electric Double-Layer Capacitors. *ChemSusChem* **2015**, *8* (11), 1875–1884. https://doi.org/10.1002/cssc.201500122.

(95) Brunauer, S.; Emmett, P. H.; Teller, E. Adsorption of Gases in Multimolecular Layers. *J Am Chem Soc* **1938**, *60* (2), 309–319. https://doi.org/10.1021/ja01269a023.

(96) Hanaor, D. A. H.; Ghadiri, M.; Chrzanowski, W.; Gan, Y. Scalable Surface Area Characterization by Electrokinetic Analysis of Complex Anion Adsorption. *Langmuir* **2014**, *30* (50), 15143–15152. https://doi.org/10.1021/la503581e.

(97) Thommes, M.; Kaneko, K.; Neimark, A. V.; Olivier, J. P.; Rodriguez-Reinoso, F.; Rouquerol, J.; Sing, K. S. W. Physisorption of Gases, with Special Reference to the Evaluation of Surface Area and Pore Size Distribution (IUPAC Technical Report). *Pure and Applied Chemistry* **2015**, *87* (9–10), 1051–1069. https://doi.org/10.1515/pac-2014-1117.

(98) Connelly, A. *BET surface area*. https://andyjconnelly.wordpress.com/2017/03/13/bet-surface-area/.

(99) Pumera, M. Materials Electrochemists' Never-Ending Quest for Efficient Electrocatalysts: The Devil Is in the Impurities. *ACS Catal* **2020**, *10* (13), 7087–7092. https://doi.org/10.1021/acscatal.0c02020.

(100) Wang, L.; Ambrosi, A.; Pumera, M. "Metal-Free" Catalytic Oxygen Reduction Reaction on Heteroatom-Doped Graphene Is Caused by Trace Metal Impurities. *Angewandte Chemie* **2013**, *125* (51), 14063–14066. https://doi.org/10.1002/ange.201309171.

(101) Cheng, F.; Su, Y.; Liang, J.; Tao, Z.; Chen, J. MnO2-Based Nanostructures as Catalysts for Electrochemical Oxygen Reduction in Alkaline Media. *Chemistry of Materials* **2010**, *22* (3), 898–905. https://doi.org/10.1021/cm901698s.

(102) Toh, R. J.; Poh, H. L.; Sofer, Z.; Pumera, M. Transition Metal (Mn, Fe, Co, Ni)-Doped Graphene Hybrids for Electrocatalysis. *Chem Asian J* **2013**, *8* (6), 1295–1300. https://doi.org/10.1002/asia.201300068.

(103) Parvez, K.; Yang, S.; Hernandez, Y.; Winter, A.; Turchanin, A.; Feng, X.; Müllen, K. Nitrogen-Doped Graphene and Its Iron-Based Composite as Efficient Electrocatalysts for Oxygen Reduction Reaction. *ACS Nano* **2012**, *6* (11), 9541–9550. https://doi.org/10.1021/nn302674k.

(104) Wang, L.; Pumera, M. Residual Metallic Impurities within Carbon Nanotubes Play a Dominant Role in Supposedly "Metal-Free" Oxygen Reduction Reactions. *Chemical Communications* **2014**, *50* (84), 12662–12664. https://doi.org/10.1039/c4cc03271c.

(105) Luxa, J.; Mate, S.; Kuc, J.; Sedmidubsky, D.; Maza, V.; Pumera, M. Ultrapure Graphene Is a Poor Electrocatalyst: Definitive Proof of the Key Role of Metallic Impurities in Graphene-Based Electrocatalysis. *ACS Nano* **2019**, *13*, 1574–1582. https://doi.org/10.1021/acsnano.8b07534.

(106) Cruz, S. M.; Schmidt, L.; Nora, F. M. D.; Pe-, M. F.; Bizzi, C. A.; Barin, J. S.; Flores, E. M. M. Microwave-Induced Combustion Method for the Determination of Trace and Ultratrace Element Impurities in Graphite Samples by ICP- OES and ICP-MS. *Microchemical Journal* **2015**, *123*, 123, 28–32. https://doi.org/10.1016/j.microc.2015.05.008.

(107) Resano, M.; Aramendía, M.; García-Ruiz, E.; Bazo, A.; Bolea-Fernandez, E.; Vanhaecke, F. Living in a Transient World: ICP-MS Reinvented via Time-Resolved Analysis for Monitoring Single Events. *Chemical Science*. Royal Society of Chemistry 2022. https://doi.org/10.1039/d1sc05452j.

(108) Stokes, D. J. *Principles and Practice of Variable Pressure/Environmental Scanning Electron Microscopy (VP-ESEM)*; 2008. https://doi.org/10.1002/9780470758731.

(109) Suzuki, E. High-Resolution Scanning Electron Microscopy of Immunogold-Labelled Cells by the Use of Thin Plasma Coating of Osmium. *J Microsc* **2002**, *208* (3), 153–157. https://doi.org/10.1046/j.1365-2818.2002.01082.x.